REE patterns of microbial carbonate and cements from Sinemurian (Lower Jurassic) siliceous sponge mounds (Djebel Bou Dahar, High Atlas, Morocco)

Giovanna Della Porta[1], Gregory E. Webb[2] & Iain McDonald[3]

1: Earth Sciences Department, Milan University, 20133 Milan, Italy (giovanna.dellaporta@unimi.it)

2: School of Earth Sciences, The University of Queensland, QLD 4072 Brisbane, Australia (g.webb@uq.edu.au)

3: School of Earth and Ocean Sciences, Cardiff University, CF10 3AT Cardiff, UK (mcdonaldi1@cardiff.ac.uk)

Keywords: Rare earth elements; Early Jurassic seawater; carbonates; microbialites; diagenesis; sedimentary contaminants

ABSTRACT

Marine microbialites serve as robust seawater rare earth element and yttrium (REE+Y) proxies through many intervals of Earth history, but questions remain about the partitioning of REEs into different coeval carbonate phases, potential syn-depositional contaminants and elemental redistribution during diagenesis. Microbial carbonates, cements and background sediments were analysed for stable isotopes (O, C) and trace element geochemistry in Sinemurian (Lower Jurassic) mid- to outer ramp siliceous sponge microbial mounds from the High Atlas, Morocco. Trace elements were analysed using laser ablation-inductively coupled plasma-mass spectrometry. Microbialites, non-luminescent radial/radiaxial fibrous (RF) cement and well-preserved brachiopods have stable isotope values similar to published Early Jurassic marine values. Luminescent blocky sparite (BS) cements have lighter stable isotope values consistent with burial

diagenesis. Early marine RF cement has shale-normalized (subscript $_{sn}$) REE+Y patterns with characteristics of oxygenated seawater, whereas cavity-occluding BS cement has high concentration bell-shaped $(REE+Y)_{sn}$ patterns, very unlike seawater. Allomicrite has relatively high REE concentrations with flatter $(REE+Y)_{sn}$ patterns. Microbialites include three subclasses distinguished on the basis of petrography and $(REE+Y)_{sn}$ patterns. Clotted peloidal microbialites (MC1) have $(REE+Y)_{sn}$ patterns broadly consistent with seawater, but with variable Ce anomalies and higher concentrations and slightly less LREE depletion relative to RF cements. Other clotted peloidal to leiolitic microbialites (MC2) have flatter $(REE+Y)_{sn}$ patterns and variable Ce anomalies, whereas leiolitic microbialites (MC3) have patterns similar to allomicrite. Hence, MC1 microbialites and early marine RF cements preserved seawater-like REE+Y patterns despite subsequent diagenesis, confirming that Early Jurassic marine REE distributions were similar to late Palaeozoic, Late Jurassic and Holocene distributions. Importantly, LREE enrichment in allomicrite and some microbialites (MC2, MC3) highlights the occurrence of LREE-enriched components that may represent marine particulate matter that preferentially scavenged LREEs from the water column prior to sedimentation. The Sinemurian siliceous sponge microbial mounds accumulated in well-oxygenated settings rather than on the edge of an oxygen minimum zone. Some of the high Ce contents in the microbialites may reflect redistribution of Ce during earliest diagenesis in suboxic pore fluids, or incorporation of LREE enriched particles or LREE uptake in the growing microbialite consistent with scavenging on organic ligands in the biofilm itself. This study demonstrates how various sedimentary sources and diagenetic processes can significantly affect otherwise robust marine REE patterns in microbial mounds within a relatively siliciclastic-free carbonate environment.

1. Introduction

The distribution and behaviour of aqueous rare earth elements and yttrium (REE+Y) have significantly improved the understanding of processes and water chemistry in natural water bodies (Elderfield and Greaves, 1982; Elderfield, 1988; Byrne and Kim, 1990; German and Elderfield, 1990; Elderfield et al., 1990; Zhang and Nozaki, 1996, 1998; Holser, 1997; Alibo and Nozaki, 1999, 2004; Nozaki and Alibo, 2003a,b). Understanding the REE distribution of seawater through time has allowed useful observations of interactions and relationships of the atmospheric-lithospheric-oceanic system through time (e.g., Kamber, 2010), because the behaviour of Ce may be used to interpret oxygenation levels (Derry and Jacobsen, 1990; German and Elderfield, 1990). Additionally, where precipitates are known to be of marine origin *a priori*, divergence from a marine pattern may inform interpretations of subsequent diagenetic processes or pathways (Rachidi et al., 2009; Webb et al., 2009; Azmy et al., 2011; Webb et al., 2012). Over the last decades, REE+Y concentrations of both modern and ancient carbonate successions, and particularly microbialites, have been successfully used to interpret the nature of seawater and lacustrine waters (Webb and Kamber, 2000; Barrat et al., 2000; Kamber and Webb, 2001; Kamber et al., 2004; Shields and Webb, 2004; Van Kranendonk et al., 2003; Bolhar et al., 2004; Cabioch et al., 2006; Olivier and Boyet, 2006; Bolhar and Van Kranendonk, 2007; Allwood et al., 2010; Webb and Kamber, 2011), palaeogeography (Nothdurft et al., 2004; Frimmel, 2009), the origin of microbialites (Guido et al., 2011; Corkeron et al., 2012), and diagenetic processes (Banner et al., 1988; Banner and Hanson, 1990; Rachidi et al., 2009; Webb et al., 2009).

It was previously suggested, on the basis of REE+Y patterns preserved in marine phosphates (fish, reptile teeth and conodonts), that REE geochemistry may have varied significantly through time and that heavy REE (HREE) depletion in Jurassic fish and reptile teeth may have been a characteristic of pre-Cenozoic seawater (Grandjean-Lécuyer et al., 1993; Picard et al., 2002; Lécuyer et al., 2004). However, marine phosphates obtain the majority of their REEs from diagenetic pore fluids (Reynard et al., 1999) and differential release of REEs in pore fluids below the sediment water interface varies depending on factors that include organic matter content,

oxygen levels, and Fe and Mn oxide content (Haley et al., 2004; Di Leonardo et al., 2009). Shields and Webb (2004) suggested that marine REE patterns have changed little through the Phanerozoic and that data from ancient phosphates (in particular biogenic) are unreliable as seawater proxies. Additionally, various studies have shown that apart from the Ce anomaly, which depends fundamentally on oxygenation levels, and Eu levels that may reflect differences in hydrothermal input, seawater REE geochemistry has been similar back to the Archean (Bau and Möller, 1993; Van Kranendonk et al., 2003; Bolhar et al., 2004; Olivier and Boyet, 2006; Frei and Polat, 2007; Kamber, 2010). Nevertheless, questions remain regarding the presence of subtle differences in marine REE geochemistry through time and, in particular, regarding how original marine REE distributions may be altered by differences in primary precipitation processes, incorporation of coeval sedimentary contaminants in different environments and subsequent diagenetic addition or redistribution of elements.

This study aims to elucidate the geochemistry of carbonates within upper Sinemurian (Lower Jurassic) microbial mounds from a carbonate ramp setting cropping out in the Djebel Bou Dahar (DBD), in the High Atlas of Morocco. Various coeval carbonate components (e.g., cements, microbial carbonate, allomicrite) were analysed from diverse carbonate facies using laser ablation-inductively coupled plasma-mass spectrometry (LA-ICP-MS). The terms ‘microbialite’ and ‘microbial carbonate’ refer to carbonate precipitates localised by benthic microbial communities or organic substances in biofilms along with any trapped and bound detritus (cf. Burne and Moore, 1987). Such carbonate precipitation may be influenced by the presence of organic matter that is not necessarily provided by microbial mats or mediated by microbial processes, such as degrading siliceous sponge bodies (Reitner, 1993; Neuweiler et al., 1999; Neuweiler et al., 2001). Hence, many of the mound carbonate samples could be labelled by the more general term automicrite, coined for autochthonous fine grained carbonate precipitate (Reitner et al., 1995). The distinction between microbialite, which is a precipitated major component of the microbial mounds, and allomicrite (carbonate mud that represents transported particulate sediment from a variety of

sources) is important because the former provides information about seawater chemistry and different processes of REE uptake at the time of precipitation, whereas the latter may or may not. Previous REE+Y data from Lower Jurassic successions in the central High Atlas rift basin (Wilmsen and Neuweiler, 2008) mostly represent whole rock solution ICP-MS analyses that diverge from seawater-like patterns with significant middle REE (MREE) enrichment. Despite the non-seawater-like nature of the patterns, Wilmsen and Neuweiler (2008) used, in part, Ce anomalies in those rocks to interpret evolving local seawater oxygenation levels through the Lower Jurassic succession. Geochemical studies of Upper Jurassic microbialites from western Europe (western Tethys and Atlantic margin, Olivier and Boyet, 2006) documented well-preserved seawater-like patterns in coral-microbialite reefs from isolated pure carbonate lagoonal settings, but found that siliciclastic contamination dominated patterns in microbialites from shallow, mixed ramp settings and affected even sponge-microbialite bioherms in deeper carbonate-dominated shelf to epicontinental basin settings. Olivier and Boyet (2006) concluded that Jurassic marine microbialites are reliable proxies of ancient seawater geochemistry but emphasised that even small amounts of terrigenous material can alter the REE signatures of microbialites. Intra-reef and carbonate detrital sediments (i.e., allomicrite) are even more subject to contamination by terrigenous sediment than microbialite (Olivier and Boyet, 2006). Hence, the DBD upper Sinemurian mounds provide a good natural laboratory to investigate Early Jurassic seawater in marine precipitates and the geochemical effects of incorporation of detrital components and early and late diagenetic alteration in such limestones, in a relatively clean carbonate setting.

2. Geological setting

The Djebel Bou Dahar (DBD) carbonate platform developed during the Early Jurassic in a marine rift basin located in the eastern portion of the High Atlas (SE Morocco; Latitude 32° 19' 30" N; Longitude 3° 7' 53" W; Fig. 1a). The carbonate depositional system formed on a fault block

controlled by E-W oriented listric faults and its evolution was affected by extensional tectonics, sea-level fluctuations and changes in the carbonate producing factory (cf. Merino-Tomé et al., 2012; Della Porta et al., 2013). The High Atlas marine rift basin included several carbonate systems developed on fault blocks, including the Rich block platform, nearly one hundred kilometres to the west of the DBD, which was investigated geochemically by Wilmsen and Neuweiler (2008). Lower Jurassic trace element data reported from the Middle Atlas (Aït Moussa) represent younger hemipelagic marls and argillaceous limestone (Pliensbachian-lowermost Toarcian) deposited on top of displaced platform successions following tectonic reorganization (Rachidi et al., 2009).

The DBD depositional geometry evolved from a low-relief ramp profile (Hettangian-Sinemurian *p.p.*) to a high-relief isolated platform with slopes dipping 19°-32° and 450-600 m in relief (latest Sinemurian-Pliensbachian; Verwer et al., 2009a, b; Merino-Tomé et al., 2012). During the late Sinemurian (Sequence III; Fig. 1b) siliceous sponge microbial mounds accumulated in middle to outer ramp settings, in water depths of 70-160 m (Della Porta et al., 2013). In the distal parts of the northern margin, where steepened slope geometry (7°-12°) developed because of fault structural control, mounds accumulated along the slope, in a similar depth range as in the southern low-angle hanging wall margin (Fig. 1b).

Siliceous sponge microbial mounds (a few metres to 15 m thick on average; Fig. 2a) nucleated on, and were surrounded by, coated-grain skeletal intraclast packstone to grainstone (Fig. 2b). Mounds consisted of: 1) *in situ* precipitated micrite and microsparite (nearly 60 %) interpreted as microbial carbonates (Fig. 2c, d); 2) centimetre-sized stromatactis-like cavities, lined by radial fibrous and radiaxial fibrous cement, and finally occluded by blocky sparite cement (Fig. 2e, f); c) variable percentages (20-40 %) of skeletal components dominated by siliceous sponge spicules (lithistid and non-rigid demosponges, hexactinosa and lyssacinosa hexactinellids), *Terebella* agglutinated worm tubes, serpulids, *Radiomura cautica*, brachiopods, molluscs and echinoderms (cf. Della Porta et al., 2013).

3. Methods

The mounds were investigated through field-based stratigraphic and sedimentological methods and optical petrography, scanning electron microscopy (SEM), fluorescence microscopy and cathodoluminescence (CL) analyses of thin sections and polished slabs. Some thin sections were stained with alizarin red and potassium ferricyanide to identify dolomite and ferroan calcite, respectively. SEM analyses were performed on gold coated polished slabs and freshly broken surfaces with a Cambridge Stereoscan 360, operating at 20 kV with working distance of 15 mm at the University of Milan, Earth Sciences Department. Cathodoluminescence was performed with a luminoscope CITL Cambridge Image Technology Limited, Cambridge, UK (model MK 5-2 operating system at 10-14 kV with a beam current between 300-600 µA, and vacuum gauge 50-70 millitor) at the University of Milan.

The different categories of carbonate precipitates identified with petrographic investigation were analysed for stable isotope and trace element geochemistry. Stable isotopes (oxygen and carbon) were analysed using a Thermo Electron Delta V advantage mass spectrometer with automated carbonate preparation device (Gas bench III) at Cardiff University, School of Earth and Ocean Sciences stable isotope facility. Carbonate powders were reacted with 100% phosphoric acid at 70°C. Stable isotope results were calibrated to the V-PDB scale using international standard NBS19. The analytical precision is better than ±0.1 % for both $\delta^{18}O$ and $\delta^{13}C$. Thirty-eight powder samples (Supplementary Online Information Table 1) were obtained using a microdrill on polished slabs selecting representative samples of radial and radiaxial fibrous cement (3 samples), blocky sparite cement (4 samples), allomicrite and peloids (11 samples), microbialite (12 samples), dolomite (1 sample) and brachiopod shells (7 samples).

Sixteen thin sections, nearly 100 µm thick, were prepared for trace element analysis using LA-ICP-MS. Following petrographic observation, each thin section was marked using a pencil drawing a circle and number in the area of interest for sampling by ablation (Supplementary Online

Information Fig. 1). Five sampling categories were selected matching the carbonate components identified through petrographic analysis and ablated for trace element analysis (Supplemental Online Information Table 2): 1) radial and radiaxial fibrous cement (17 measurements), 2) blocky sparite cement (9 measurements), 3) allomicrite (11 measurements), 4) clotted peloidal, laminated and leiolitic microbialite (36 measurements), and 5) saddle dolomite in voids (2 measurements). Analyses were carried out at the School of Earth and Ocean Sciences, Cardiff University, UK, using a Thermo X(7) series ICP-MS coupled to a New Wave Research UP213 UV laser. The laser spot diameter was 100 µm and laser energy was ~7 mJ with a pulse rate of 4 Hz. Helium gas was used as a carrier from the laser cell and this was combined with Argon outside the cell as the sample was transported to the ICP-MS. Thermo Plasmalab time-resolved analysis (TRA) data acquisition software was used with a total acquisition time of 90s per analysis, allowing 20s for background to produce a gas blank for blank subtraction followed by 60s for laser ablation and 10s signal washout. The isotopes used for analysis were ^{24}Mg, ^{27}Al, ^{29}Si, ^{44}Ca, ^{51}V, ^{53}Cr, ^{55}Mn, ^{59}Co, ^{62}Ni, ^{65}Cu, ^{68}Zn, ^{88}Sr, ^{89}Y, ^{90}Zr, ^{95}Mo, ^{111}Cd, ^{118}Sn, ^{121}Sb, ^{139}La, ^{140}Ce, ^{141}Pr, ^{146}Nd, ^{147}Sm, ^{153}Eu, ^{157}Gd, ^{159}Tb, ^{163}Dy, ^{165}Ho, ^{166}Er, ^{169}Tm, ^{172}Yb, ^{175}Lu, ^{232}Th and ^{238}U. The first 10 seconds of each ablation was ignored to avoid any surface contamination. The signal for ^{29}Si was used to monitor whether the ablation continued into the underlying glass slide and the integration window was stopped at a point at least 5 seconds from where the ^{29}Si signal rises dramatically due to input from the glass. Typically this produced a clean carbonate integration window of 25-35 seconds. Plasmalab software was used for initial data reduction with post-processing in Excel. The calibration employed NIST614, NIST612 and NIST610 reference glasses to produce a 4 point (including the origin) calibration curve. Data were normalised to Ca (assuming pure $CaCO_3$) and adjusted accordingly. Instrumental drift was monitored by repeated analysis of NIST612 after every 10 unknowns. Certified carbonate reference standards were not available and the accuracy of the analyses was assessed using basalt glass standard BIR-2g. Differences between the measured and certified values for BIR-2g varied between 1-20 % and were consistently < 10 % for rare earths with the exception of La. Some locations were

sampled with 2 or 3 spots to verify the consistency of the measurements. Precision measured by repeatability between closely spaced laser spots was < 20 %, and more commonly < 10 %, for the rare earths, Sr and Y. Precision for other elements varied more widely from < 1 to > 50 % depending on the concentration and the homogeneity of the element within the carbonate matrix. Analytical uncertainty of the measurements was < 10 % for most of the trace elements with exception of La and Th for which it was 10-20 %. Following the LA-ICP MS measurements, selected thin sections were ground to 30 µm thickness to evaluate the sampled spots through additional petrographic analysis (Supplementary Online Information Fig. 1).

REE concentrations (Table 2, Supplementary Online Information Table 2) are expressed normalized to 'Mud from Queensland' (MuQ) of Kamber et al. (2005), a modern alluvial sediment composite that here serves for traditional shale normalisation (e.g., PAAS – Post-Archean Average Australian Shale; McLennan 1989) with normalized values expressed as $(REE)_{sn}$, The ratio $(Nd/Yb)_{sn}$ was calculated to monitor light REE (LREE) depletion. The ratio $(Dy/Yb)_{sn}$ was calculated to monitor heavy REE (HREE) depletion. Y was inserted into the REEs between Dy and Ho, according to its effective ionic radius in order to monitor detrital clastic contamination. The majority of geologic materials (including all volcanic rocks and siliciclastic sediments) have near chondritic values of Y/Ho around 24-34, whereas modern seawater has Y/Ho ratio > 44 (Bau, 1996; Nozaki et al., 1997). MuQ-normalised anomalies were calculated using the formula $(Ln/Ln^*)_{sn}$ with Ln* following the geometric formulas of Lawrence et al. (2006): with $(La^*)_{sn} = Pr_{sn}*(Pr_{sn}/Nd_{sn})^2$; $(Ce^*)_{sn} = Pr_{sn}*(Pr_{sn}/Nd_{sn})$; $(Eu^*)_{sn} = (Sm_{sn}^2*Tb_{sn})^{1/3}$; and $(Gd^*)_{sn} = (Tb_{sn}^2 * Sm_{sn})^{1/3}$.

4. Results and Interpretations

4.1. Petrography of carbonate precipitates

4.1.1. Description

Petrographic, SEM and CL investigations allowed the identification of four main categories of carbonate precipitates within the upper Sinemurian mounds and surrounding coated grain skeletal packstone-grainstone. These categories are: 1) radial and radiaxial fibrous cement (RF cement), 2) blocky sparite cement (BS cement) and rare calcite-replacing saddle dolomite, 3) allomicrite with peloids, and 4) microbialites with different fabrics, ranging from clotted peloidal micrite and microsparite to structureless leiolite, associated with siliceous sponge bodies, loose spicules and various sparse skeletal fragments.

The inclusion-rich RF cement is non-luminescent (Supplementary Online Information Fig. 2a-b) as are the sparse brachiopod shells. The limpid BS cement stains blue with potassium ferricyanide (Fig. 2f). In CL it reveals alternating generations of non-luminescent and luminescent scalenohedral cement followed by luminescent (Mn- and Fe-rich) cement (Supplementary Online Information Fig. 2c-d). Allomicrite, within the coated grain skeletal packstone, has blotchy luminescence (Supplementary Online Information Fig. 2e-f) as do peloids. Reworked sponge spicules are partly luminescent within the allomicrite, whereas sponge spicules within mound intraclasts embedded in microbial clotted peloidal micrite are non-luminescent.

CL of the microbialites varies from non-luminescent to blotchy luminescence (Supplementary Online Information Fig. 3a-b). The worm tube *Terebella* is luminescent (Supplementary Online Information Fig. 3c-d), probably because of the agglutinating nature of its shell, which incorporates external particles and potentially organic matter (Guido et al., 2014). The leiolitic microbialite shows local enrichments in Fe and Mn oxides and has patchy luminescence, but the embedded calcified siliceous sponge spicules are non-luminescent (Supplementary Online Information Fig. 3e-f). Locally there are non-luminescent idiomorphic quartz crystals and saddle dolomite crystals in fractures. None of the samples analysed showed significant fluorescence.

4.1.2. Interpretation

The four distinct categories of carbonate precipitates represent both primary sedimentary and diagenetic features, but these are not discussed below in a chronological paragenetic sequence.

On the basis of morphology and non-luminescence, RF cements are interpreted as early marine cements, whereas the cavity-occluding limpid BS cement is interpreted as later stage burial cement, on the basis of zoned luminescence, which suggests high Mn content, and staining consistent with burial ferroan calcite. The variable CL behaviour of the microbialites probably reflects non-uniform burial diagenetic overprint and/or presence of minor organic matter, although no samples fluoresce. Modern reefal microbialites are irregularly porous (Webb et al., 1998; Camoin et al., 1999), allowing variable mixtures of early marine and later pore-occluding cements to become incorporated. The non-luminescence of the calcite-replaced sponge spicules embedded in microbial carbonate suggests that silica dissolution and calcite replacement occurred during early marine diagenesis. A similar situation was documented in Mississippian sponge-microbial mounds wherein lithistid sponges encrusted by microbialites contained spicule moulds that were partially filled by fine geopetal sediment while still on the seafloor (Webb, 1999). In contrast, the isolated, reworked sponge spicules within the coated grain packstone surrounding the mounds show luminescence, probably reflecting subsequent diagenesis in a burial environment. The very early formation of siliceous sponge spicule moulds is clear evidence that mound microbialites precipitated as rigid structures on the seafloor.

Idiomorphic quartz and saddle dolomite are interpreted to have late diagenetic origins, likely related to hydrothermal fluids as suggested in the Middle Atlas Pliensbachian-Toarcian marls by Rachidi et al. (2009). The DBD younger (Pliensbachian) platform succession is characterized by Mississippi Valley Type (MVT) Pb-Zn ores attributed to the mixing of a high-temperature saline fluid (180° C, > 25 wt % NaCl equivalent) derived from halite-dissolution, and a cooler, less saline fluid (70° C, 16 wt % NaCl equivalent) related to evaporated seawater (Adil et al., 2004). It is possible that hydrothermal fluids also affected the upper Sinemurian mound strata in some areas.

4.2. Stable isotope data

4.2.1. Description

Mean stable isotope data from RF cement (Table 1, Supplementary Online Information Table 1; Fig. 3) are 2.3 ‰ for $\delta^{13}C$ and -1.6 ‰ for $\delta^{18}O$, while brachiopods at the top of the siliceous sponge microbial mounds have mean $\delta^{13}C$ values of 2.2 ‰ and -2.7 ‰ for $\delta^{18}O$. BS cements have mean values of 2.1 ‰ for $\delta^{13}C$ and -5.5 ‰ for $\delta^{18}O$; one sample of saddle dolomite associated with the BS in a void provides values of 0.4 ‰ for $\delta^{13}C$ and -5.5 ‰ for $\delta^{18}O$. Allomicrite has mean values of 1.9 ‰ for $\delta^{13}C$ and -3.9 ‰ for $\delta^{18}O$, whereas microbial carbonate has similar mean values to the RF cement and brachiopods with $\delta^{13}C$ of 2.3‰ and $\delta^{18}O$ of -2.7 ‰.

4.2.2. Interpretation

Brachiopod shell, RF cement and microbialite stable isotope values fall within the field of stable isotope signatures for Lower Jurassic marine limestones, approximately within the ranges of 0.4 ‰ and 3.2 ‰ for $\delta^{13}C$ and -0.2 ‰ and -3.3 ‰ for $\delta^{18}O$ (Fig. 3; cf. Veizer et al., 1999; Rosales et al., 2001; Wilmsen and Neuweiler, 2008). These isotope values further support the interpretation of marine origin for the RF cements suggested by the non-luminescence and crystal shape. Microbialite also has a marine isotopic signal overlapping with the brachiopod values, RF cement and values from published literature. The analysed microbialites do not appear to show isotopic evidence of enzymatic fractionation related to microbial respiration or photosynthesis. They are, therefore, consistent with those microbialites in modern reef settings and from the geological record that do not display biologically mediated fractionation of oxygen and carbon stable isotopes (Keupp et al., 1993; Reitner et al., 1995; Camoin et al., 1999) suggesting that their precipitation occurred in

equilibrium with seawater. In modern microbialites, bacterial photosynthesis, microbial respiration and sulphate reduction could produce isotope fractionation with a ~1 ‰ shift of $\delta^{13}C$ (Londry and Des Marais, 2003; Andres et al., 2006; Heindel et al., 2010). However, such a shift might not be easily detected in ancient microbialites such as those measured here.

The significantly lighter oxygen isotope ratios of the BS cements and saddle dolomite are consistent with precipitation in the late burial environment. The allomicrite samples range between more marine and more burial diagenetic values, whereas, the microbial carbonate values do not indicate evidence of significant diagenetic alteration in burial or meteoric diagenetic environments.

4.3. Rare Earth Element and Yttrium Geochemistry

Trace element data, significant ratios and anomalies for each analysed sample are shown in Supplementary Online Information Table 2, while mean values for distinct carbonate categories are summarised in Table 2. The MuQ-normalised REE+Y distributions of each category of carbonate precipitate identified through petrographic and CL analysis are distinct (Figs. 4-6). $(REE+Y)_{sn}$ patterns combined with petrography allow the microbialites to be subdivided into three subcategories for a total of seven distinct categories. Trace element results are discussed separately for each category: 1) RF cement; 2) BS cement; 3) allomicrite within coated grain skeletal packstone - AL; 4) clotted peloidal micrite microbialite (microbialite type 1 – MC1); 5) clotted peloidal to leiolitic microbialite (microbialite type 2- MC2); 6) leiolitic microbialite with sparse peloids and skeletal fragments (microbialite type 3- MC3); and 7) burial saddle dolomite.

4.3.1. Radial/radiaxial fibrous (RF) cement

RF cement samples (n = 17) have $(REE+Y)_{sn}$ patterns (Fig. 5a) characterised by: relatively low concentrations (mean ΣREE = 1.94 ppm; standard deviation SD = 1.18 ppm; range: 0.36 to

4.81 ppm); significant LREE depletion [mean $(Nd/Yb)_{sn}$ = 0.2, SD = 0.06]; superchondritic Y/Ho ratio (mean Y/Ho = 78.56, SD = 15.37); positive La and Gd anomalies (mean $(La/La^*)_{sn}$ = 3.65, SD = 0.95; mean $(Gd/Gd^*)_{sn}$ = 1.3, SD = 0.41); and negative Ce anomalies (mean $(Ce/Ce^*)_{sn}$ = 0.65, SD = 0.16; Fig. 7). Eu anomalies are small to absent ($(Eu/Eu^*)_{sn}$ = 1.08, SD = 0.2). Al_2O_3 and Th occur in traces (0.004 % weight and 0.004 ppm, respectively), while Zr is 0.63 ppm (SD = 0.17). Concentrations of U (mean U = 0.06 ppm; SD = 0.01 ppm) and Mn (mean Mn = 106.58 ppm, SD = 64.02) are also low, but variable. These data are consistent with relatively well-preserved marine cement that lacks significant siliciclastic contamination, consistent with petrographic, CL and stable isotope interpretations.

4.3.2. Blocky sparite (BS) cement

BS cement samples (n = 9) have bell-shaped $(REE+Y)_{sn}$ patterns (Fig. 5b) with very high REE concentrations relative to RF cement (mean ΣREE = 22.23 ppm, SD = 7.46 ppm) ranging from 8.28 to 31.27 ppm. The REE distribution is MREE enriched [mean $(Nd/Yb)_{sn}$ =1.64, SD = 0.39] with variable Y/Ho ratios ranging from 36.33 to 64.08 (mean Y/Ho = 47.07, SD = 9.75). The HREEs consistently decline in concentration with increasing mass, unlike all other analysed samples. The Ce anomalies are mostly negative but $(Ce/Ce^*)_{sn}$ ranges from 0.61 to 1.33 with two out of nine values being positive (Fig. 7). However, the single positive Ce anomaly that cannot be explained within the 10% analytical precision has a lower than expected Pr value based on the trend from Sm to Nd, and hence may be anomalously high owing to the nature of the anomaly calculation. Excluding that value, mean $(Ce/Ce^*)_{sn}$ = 0.87 (SD = 0.14). The La anomalies are more variable with five positive and four negative values ($(La/La^*)_{sn}$ = 0.44-1.67). The Eu anomalies are largely positive (mean $(Eu/Eu^*)_{sn}$ = 1.23, SD = 0.27), but Gd anomalies are ~1 (mean $(Gd/Gd^*)_{sn}$ = 1.06, SD = 0.11). Concentrations of Al_2O_3, Zr and Th are very low with mean values of 0.001 % weight, 0.06 ppm, and 0.01 ppm, respectively, consistent with a lack of direct siliciclastic

contamination. U concentrations are also extremely low (mean U = 0.004 ppm; SD = 0.003 ppm) but Mn values are higher but highly variable (mean Mn = 538.28 ppm; SD = 420.71 ppm) consistent with CL analyses. Although many of the patterns have high Y/Ho ratios and negative Ce anomalies, they differ significantly as a group from seawater REE distributions, and appear to reflect more than one subsequent burial fluid.

4.3.3. Allomicrite (AL)

AL samples (n = 11) have flat $(REE+Y)_{sn}$ patterns (Fig. 5c). REE concentrations are relatively high (mean ΣREE = 13.33 ppm, SD = 6.74 ppm), but variable, ranging from 4.30 to 26.49 ppm. The flat pattern reflects LREE enrichment relative to hypothetical seawater but most samples still have some LREE depletion overall [mean $(Nd/Yb)_{sn}$ = 0.80, SD = 0.12]. Y/Ho ratios are relatively low, ranging from 37.40 to 58.18 (mean Y/Ho = 47.34, SD = 6.46) and the Ce anomaly is mostly negative (mean $(Ce/Ce^*)_{sn}$ = 0.89, SD = 0.08), but with two samples with Ce anomalies ~1. The La anomaly is positive (mean $(La/La^*)_{sn}$ = 1.39, SD = 0.19) as well as most of the Eu anomalies, however, one Eu anomaly is negative and two are around 0.9 (mean $(Eu/Eu^*)_{sn}$ = 1.11, SD = 0.15). The Gd anomaly is mostly ~1. Mean Al_2O_3 content is 0.33 % weight, while mean Zr is 3.22 ppm (SD = 1.95) and mean Th is 0.33 ppm (SD = 0.12). Mn concentrations are variable (mean Mn = 241.17 ppm; SD = 73.58 ppm). Some AL $(REE+Y)_{sn}$ patterns have aspects of seawater distribution, but they are clearly distinguishable from the seawater-like RF cements on the basis of higher REE concentrations and reduced LREE depletion. Increased Al_2O_3, Zr and Th concentrations (Table 2) suggest minor direct siliciclastic contamination.

4.3.4. Microbialites

The *in situ* precipitated carbonates, which are major mound constituents and interpreted as microbially mediated/influenced precipitates, have highly variable microstructures (from clotted peloidal to leiolitic micrite or microspar) and variable $(REE+Y)_{sn}$ patterns. Microbialites were separated into the following groupings (Fig. 5d-f): a) clotted peloidal micrite with seawater-like $(REE+Y)_{sn}$ patterns (microbialite type 1, MC1); b) clotted peloidal to leiolitic microbialite with flattened $(REE+Y)_{sn}$ patterns (microbialite type 2, MC2); and c) leiolitic microbialite containing sparse peloids, skeletal fragments and probably associated allomicrite with flattened $(REE+Y)_{sn}$ patterns (microbialite type 3, MC3).

4.3.4.1. Microbialite type 1 (MC1)

Fifteen MC1 samples (Fig. 5d) have mean ΣREE of 5.23 ppm (SD = 4.44) ranging between non-cohesive patterns with ΣREE of 0.77 ppm and cohesive patterns with ΣREE of 14.23 ppm. REE+Y concentrations of MC1 samples are characterised by: strong LREE depletion [mean $(Nd/Yb)_{sn}$ = 0.31, SD = 0.11]; superchondritic Y/Ho ratios (mean Y/Ho = 67.13, SD = 13.96, range 48.3-97.05); variable Ce anomalies (Fig. 7) with 10 out of 15 being negative (mean $(Ce/Ce^*)_{sn}$ = 0.72, SD = 0.26), but five samples basically lacking Ce anomalies with values between 0.95 and 1.08; consistent positive La anomalies (mean $(La/La^*)_{sn}$ = 2.85, SD = 1.49); and more variable Eu and Gd anomalies. Lithophile elements and terrigenous indicators occur in low concentrations (mean Al_2O_3 is 0.03 % weight, mean Zr = 0.9 ppm, mean Th = 0.07 ppm). Mn concentrations are variable (mean Mn = 145.03 ppm; SD = 77.15 ppm) and U concentrations are low (mean U = 0.07 ppm; SD = 0.02 ppm). With few exceptions, MC1 carbonates have strong seawater-like REE+Y characteristics with values being most similar to the RF cement but with slightly less LREE depletion. Variations in the Ce, Eu and Gd anomalies may reflect minor diagenetic overprints, consistent with some variability in CL, or varying redox conditions in localised microenvironments where the carbonate was precipitated within the mound.

4.3.4.2. Microbialite type 2 (MC2)

Fourteen MC2 samples have flatter $(REE+Y)_{sn}$ patterns (Fig. 5e) relative to the RF cement and MC1 carbonates. As a group, they have more consistent total REE concentrations (mean ΣREE = 5.27 ppm, SD = 1.42 ppm) ranging between 2.93 and 9.33 ppm, falling mostly between values for RF cements and MC1 carbonates. However, they generally show much reduced LREE depletion with mean $(Nd/Yb)_{sn}$ = 0.62 (SD = 0.18). The Y/Ho ratio is superchondritic (mean Y/Ho = 56.82, SD = 9.32) within the marine range of 44-74 (Bau, 1996). Ce anomalies are minimal (mean $(Ce/Ce^*)_{sn}$ = 0.92, SD = 0.10), and seven samples lack an anomaly within analytical precision with $(Ce/Ce^*)_{sn}$ between 0.93 and 1.1. The La anomalies are all positive (mean $(La/La^*)_{sn}$ = 1.57, SD = 0.37), while small variable Eu and Gd anomalies vary either way. The mean Al_2O_3 content of 0.2 % weight, mean Zr = 2.61 ppm and mean Th = 0.2 ppm plot higher than MC1 samples and lower than allomicrites. Mn concentrations are variable (mean Mn = 224.69 ppm; SD = 69.26 ppm) and U are low (mean U = 0.11 ppm; SD = 0.07 ppm). Although aspects of seawater REE distribution are apparent, the flatter REE_{sn} distributions, elevated Ce concentrations and higher lithophile element content are consistent with detrital contamination and diagenetic overprints provided the initial microbialite was similar to MC1.

4.3.4.3. Microbialite type 3 (MC3)

The third discrete group of microbialite samples (MC3; n = 7) shows possible petrographic evidence of being a mixture of microbial carbonate and allomicrite because it has a structureless fabric and includes particulate material, including isolated sponge spicules, sparse skeletal grains, and peloids. These leiolitic carbonates (Fig. 5f) have relatively flat $(REE+Y)_{sn}$ patterns [mean $(Nd/Yb)_{sn}$ = 0.72, SD = 0.22] with consistently high REE concentrations (mean ΣREE = 9.96 ppm,

SD = 1.68, range 7.61-12.37 ppm). The Y/Ho ratio varies from near chondritic values (33.66) to lower marine values (53.46) (mean Y/Ho = 41.4, SD = 6.72). Ce anomalies also vary with positive values for three samples, $(Ce/Ce^*)_{sn}$ = ~1.1, and negative Ce anomalies in the range of ~0.71-0.86 for the remaining four. However, such low positive Ce anomalies (within 10 %) cannot definitively support excess Ce, given the analytical precision and anomaly calculation equation. La anomalies are positive (mean $(La/La^*)_{sn}$ = 1.48, SD = 0.23), as are most of the Eu and one of the Gd anomalies. MC3 samples show the highest concentrations of Al_2O_3 (0.48 % weight), Zr (mean = 4.91 ppm) and Th (mean = 0.41 ppm) of the measured categories. Mn concentrations are relatively low (mean Mn = 179.54 ppm; SD = 66.77 ppm); U concentrations are relatively high but variable (mean U = 0.33 ppm; SD = 0.28 ppm). The MC3 samples are consistent with precipitation from seawater, but with significant contamination from allomicrite, detrital sediment and possible overprint from diagenesis.

4.3.5. Replacive saddle dolomite

Replacive burial saddle dolomite samples (n = 2) have $(REE+Y)_{sn}$ patterns (Fig. 6) characterised by: high concentrations (ΣREE = 21.9, 22.5 ppm); LREE enrichment [$(Nd/Yb)_{sn}$ = 1.90, 1,76]; low superchondritic Y/Ho ratio (Y/Ho = 44.9, 45.5); no La or Gd anomalies; negative Ce anomalies, $(Ce/Ce^*)_{sn}$ = 0.82, 0.87, and positive Eu anomalies ($(Eu/Eu^*)_{sn}$ = 1.18, 1.25). Lithophile elements occur in traces (Al_2O_3 = 0.019, 0.035 % weight; Th = 0.012, 0.015 ppm; Zr = 2.71, 5.6 ppm) suggesting no direct siliciclastic contamination. The $(REE+Y)_{sn}$ patterns are similar overall to those of the burial BS cement, but with less MREE enrichment.

5. Sources of distinct $(REE+Y)_{sn}$ patterns

The $(REE + Y)_{sn}$ patterns of analysed Sinemurian carbonates suggest the influence of several factors, including: Early Jurassic seawater REE + Y concentrations, contamination by terrigenous sediment, possible incorporation of particulate matter containing elements scavenged from the water column, Fe and Mn oxyhydroxides, and early to late burial diagenesis. Mean $(REE+Y)_{sn}$ trends of the distinguished categories shown in Figure 6 are interpreted on the basis of the sources of REE + Y. Figure 7 shows the plots of the Ce and La anomalies.

5.1. RF cement and MC1 microbialite: seawater-like $(REE+Y)_{sn}$ patterns

The RF cement and MC1 microbial carbonates plot near each other (Figs. 5-7) and have $(REE+Y)_{sn}$ patterns, Y/Ho ratio, negative Ce anomalies, and positive La anomalies similar to modern shallow oxygenated seawater (e.g., Zhang and Nozaki, 1996). Hypothetical distribution coefficients calculated for RF cement and MC1 microbialites using modern seawater values (mean values to 200 m and 50 m depth from sites St. SA07 and St. SA12 in the south Pacific Ocean after Zhang and Nozaki, 1996) are relatively consistent across the mass range with mean $D_{RF/sw}$ = 682 (SD = 216) and mean $D_{MC1/sw}$ = 1731 (SD= 514) (Fig. 8a). These values are higher than previously determined values for Devonian marine cements (Nothdurft et al., 2004) and Holocene microbialites (Webb and Kamber, 2000). The high REE concentrations could reflect higher initial REE concentrations in the DBD Early Jurassic seawater, relative to modern Pacific Ocean seawater, but empirical and experimental distribution coefficients for REEs between seawater and carbonates have proven to be highly variable in different settings and materials (cf. Terakado and Masuda, 1988; Zhong & Mucci, 1995; Tanaka and Kawabe, 2006; Webb et al., 2009); the high values obtained are well below the experimentally calculated values of Terakado and Masuda (2006). Hypothetical distribution coefficients calculated for RF cements are relatively uniform across the mass range as in previous empirical studies, and unlike experimental results (Zhong and Mucci, 1995; Tanaka and Kawabe, 2006). If the $(REE+Y)_{sn}$ patterns of the RF cements are taken to

represent Early Jurassic seawater, the main differences between them and those of the MC1 microbialites are increased concentration, slight LREE enrichment, variable Ce anomaly, lower La anomaly and lower Y/Ho ratio in MC1 (Fig. 8b). REE distributions of MC2 and MC3 samples and allomicrite share some aspects of seawater distributions, but diverge so as to suggest incorporation of REEs from other sources (see sections 5.3 and 5.4).

5.2. BS cement: late diagenetic $(REE+Y)_{sn}$ patterns

The variability of the BS cements is consistent with more than one stage of diagenetic fluids that produced blocky calcite cement. The $(REE+Y)_{sn}$ distributions of the BS cements are broadly similar to each other with a bell-shape characterised by MREE enrichment and declining HREEs and LREEs (Figs. 5, 6). Such bell-shaped patterns are typical of diagenetically altered carbonate and phosphate deposits (Shields and Webb, 2004; Rachidi et al., 2009). Petrographic and CL analyses (luminescent blocky spar cement stained blue by potassium ferricyanide) and very low U content (some samples at or near detection limit, mean U = 0.004 ppm, SD = 0.003 ppm compared to mean U = 0.06 ppm, SD = 0.01 ppm in RF cements) suggest that the bell shape does not reflect the direct presence of phosphate minerals. Haley et al. (2004) showed similar MREE-enriched patterns in pore fluids below the sediment-water interface in marine settings and attributed them to enhanced release of MREEs from Fe-oxides in continentally derived sediments as they were reduced in anoxic pore waters. Although the BS cement is unlikely to represent early diagenesis beneath the seafloor, as supported by its light O isotopic values relative to the RF cement (Fig. 3) and sequence in pore filling, the burial fluids that affected the Upper Sinemurian carbonates may have been in contact with siliciclastic sediments or rocks that contained Fe-oxides. Himmler et al. (2010) attributed MREE enrichments in precipitates associated with cold seeps to Fe-oxide reduction in anoxic pore fluids. However, the DBD BS cement lacks the strongly negative C isotope signature of cold seep carbonate.

The variable low negative Ce anomalies of the BS cement (Fig. 7) are also consistent with burial diagenesis in dysoxic settings and with the precipitation of ferroan calcite and dolomite. As discussed above, the calculation of small Ce anomalies is complicated by the analytical precision and the extrapolation method used. In particular, small Ce anomalies are difficult to quantify in bell-shaped REE patterns. The linear extrapolation method utilised for anomaly calculation here (Lawrence et al., 2006), so as to account for the anomalous La behaviour in seawater, may not be appropriate if the REE mass relationship is not linear. Kamber et al. (2014) explored the possibility of using a polynomial function to calculate the Ce anomaly in some Archean microbialites and suggested that it may provide an explanation for apparent small positive Ce anomalies in some samples, but additional work is required. Regardless, owing to the analytical precision, the majority of small positive Ce anomalies in the present study are very close to $(Ce/Ce^*)_{sn} = 1$, and hence, although they reflect excess Ce relative to a normal oxygenated seawater source, they do not necessarily reflect excess Ce in relation to the adjacent REEs.

The positive Eu anomalies in some BS samples could have various origins. Positive Eu anomalies were identified in the MREE-enriched early pore fluids described by Haley et al. (2004), but may also reflect abundant weathering of plagioclase from a terrigenous or volcanic source (Cabioch et al., 2006) or a potential direct influence of hydrothermal fluids during burial (cf. Kamber and Webb, 2001 and references therein). The Lower Jurassic carbonates analysed here are underlain by basalts of the Central Atlantic Magmatic Province (CAMP; Marzoli et al., 2004). A late hydrothermal fluid influence is consistent with the presence of sparse saddle dolomite (which has a positive Eu anomaly; cf. Supplementary Online Information Table 2, Table 2) and idiomorphic quartz, which might be related to MVT Pb-Zn mineralization developed in younger (Pliensbachian) strata of the DBD (Adil et al., 2004). Railsback and Hood (2001) documented multistage diagenesis with meteoric calcite cements in shallower settings overlapping with burial calcite cements in deeper settings followed by later diagenesis during uplift of the High Atlas Mountains, but suggested that burial fluids did not reach metamorphic temperatures, at least

regionally. Wilmsen and Neuweiler (2008) reported a single high-concentration $(REE+Y)_{sn}$ pattern with significantly positive La and Eu anomalies and LREE enrichment from a vein calcite interpreted as a deep burial, high temperature diagenetic precipitate in the central High Atlas Rift Basin. The two late saddle dolomite samples in the present analyses both have significant LREE enrichment, but lack a strong positive La anomaly and have only a small positive Eu anomaly relative to the vein calcite of Wilmsen and Neuweiler (2008). Many of the BS cements also have $(Nd/Yb)_{sn} > 1$, but in some cases, at least, that reflects more HREE depletion than LREE enrichment in the bell-shaped patterns. Regardless, the DBD BS cements clearly reflect late stage diagenetic fluids based on their final pore filling position, and their high REE concentrations and consistent MREE enrichment allow them to serve as an end-member with which to analyse for late diagenetic cement overprint in the other mound carbonates.

5.3. Allomicrite: altered and contaminated seawater-like $(REE+Y)_{sn}$ patterns

Allomicrite and skeletal grains are patchily luminescent suggesting partial alteration during burial diagenesis. However, hypothetical mixing between the marine REE proxy, e.g., RF cement, and BS cement (Fig. 9a) does not produce the flat pattern through the LREE observed in the allomicrite. Some burial diagenetic influence may explain the small positive Eu anomaly in mean allomicrite (Table 2), but burial diagenesis does not adequately clarify the flattened $(REE+Y)_{sn}$ pattern. The relatively consistent distribution coefficients calculated for RF cements and MC1 (Fig. 8a) would seemingly preclude major differences in partitioning across the mass range, as has been suggested in some experimental work (Zhong and Mucci, 1995; Tanaka and Kawabe, 2006). Hence, AL appears to contain an additional source of REEs that was particularly enriched in LREEs. LREE-enriched late stage dolomite can be ruled out as the possible source, as it would have been visible petrographically and avoided during sample ablation. Additionally, late stage overprints were not present in many samples where laser ablation sampling sites were separated by only

millimetres (Fig. 4), but the REE patterns of the petrographically distinguished carbonate classes were still distinct. Because the additional REE source is not consistent with overprint by any of the known late stage precipitates (e.g., BS cement and saddle dolomite), it may have been incorporated within the allomicrite with the particulate sediment.

The somewhat seawater-like, but higher concentration, less LREE depleted $(REE+Y)_{sn}$ patterns of AL might partly reflect direct siliciclastic contamination as indicated by the higher concentrations of Th, Zr and Al_2O_3 (Fig. 10, Table 2). Hypothetical mixing between the marine $(REE+Y)_{sn}$ pattern inferred from mean RF cement and MuQ (Fig. 9b) suggests that the AL pattern is close to that achieved by mixing RF cement and 5 % MuQ. However, the measured concentrations of Al_2O_3, Zr and Th are too low to support such a high level of clastic contamination. The concentrations for 5 % MuQ mixed with RF cement should correspond to: Al_2O_3 0.86 % weight, Zr 9.95 ppm, Th 0.56 ppm. Some of the AL samples approach these values but others are much lower (Fig. 10) resulting in mean concentrations for AL of: Al_2O_3 0.33 % weight, Zr 3.22 ppm, Th 0.33 ppm, i.e., approximately one-third to one-half of those values. Cross plots (Fig. 11) suggest that, for some AL samples, increasing total REE concentration, decreasing LREE depletion, and decreasing Y/Ho ratio correlate with increasing Al_2O_3, Th, and Zr, consistent with some direct siliciclastic contamination. However, whereas AL concentrations of Zr and Th are correlated (R^2 = 0.63; Fig. 10c), Zr, Th and Al_2O_3 are not correlated with ΣREE (R^2 = 0.29-0.16), Y/Ho (R^2 = 0.38-0.07) and $(Nd/Yb)_{sn}$ (R^2 = 0.13-0.01; Fig. 11). Some AL samples have higher total REE concentration, less LREE depletion and lower Y/Ho ratios than can be explained exclusively by typical fluvial clastic sediment contamination alone. Hence, additional REE sources must be considered.

A possible sedimentary contaminant is aeolian dust, which is commonly enriched in LREEs to some degree (e.g., Greaves et al., 1999; Marx et al., 2005: Hongo et al., 2006; Tang et al., 2013). In some dusts, LREE enrichment reflects the preferential sorting of heavy minerals during the transport process so that many HREE-rich phases, such as Zr, are absent or scarce in the finest dust

fractions after transport (Marx et al., 2005). Rare LREE-enriched dust samples have been documented with REE concentrations as high as PAAS and MuQ (e.g., loess from Buccleuch, South Island of New Zealand, Marx et al., 2005, their fig. 3). The degree to which addition of such aeolian dust to seawater affects the seawater REE distribution has been controversial. Greaves et al. (1999) suggested that addition of aeolian dust to north Pacific seawater modified the REE patterns, with some LREE enrichment, whereas Hongo et al. (2006) reported that there was less direct effect on the surface seawater REE distributions. If a significant amount of LREE-enriched dust were introduced to seawater it would be expected to interact with the water to some degree and thus cause less LREE depletion in the water column at depth. The RF cement analysed here, which is interpreted to have been precipitated directly from the seawater, still shows very strong LREE depletion consistent with modern shallow oxygenated seawaters. Hypothetical mixing of RF cement with the aeolian dust with the highest REE content of Marx et al. (2005; i.e., their Buccleuch sample) should provide a powerful test of potential wind-blown dust contamination in the DBD samples. However, cross plots suggest that this LREE-enriched aeolian dust is an unlikely source for most of the AL samples as it would require much higher dust concentrations, and consequently abundances of Th, Zr and Al_2O_3 to achieve such high REE concentrations and reduced LREE depletion and Y/Ho ratios relative to ΣREE (Fig. 11). Note in particular that, although the LREE-enriched dust increases $(Nd/Yb)_{sn}$ more effectively than MuQ (Fig. 11d), AL plots significantly above the dust mixing line, suggesting additional LREE enrichment not linked to extraneous terrigenous sediment (aeolian or fluvial). Hypothetical mixing lines between Marx et al. (2005) loess and RF cement and MC1 microbialites also fail to account for variation in the La and Ce anomalies in AL (Fig. 12). A loess with lower REE concentrations would be expected to have even less effect on the REE distributions.

Another possible source for the AL $(REE+Y)_{sn}$ trends, which is consistent with the allomicrite depositional setting, is the incorporation of particulate matter (carbonate sediment with organic colloids and/or Fe-Mn oxyhydroxides) that preferentially scavenged LREEs from the

overlying water column before deposition on the seafloor. Removal of LREEs, relative to the more carbonate-complexed HREEs during scavenging by organic matter and particles in the water column, has been considered a primary source of LREE depletion in shallow seawater (Elderfield and Greaves, 1982; Byrne and Kim, 1990; Elderfield et al., 1990; Byrne and Lee, 1993; Sholkovitz et al., 1994; Bau, 1996; Tachikawa et al., 1999; Luo and Byrne, 2004). Although the complexed elements may be released during oxidation of organic matter in deeper seawater (Sholkovitz et al., 1994), the studied mound depositional setting is interpreted as a relatively shallow middle-outer ramp (70-160 m depth; Della Porta et al., 2013), thus providing a high contrast between the REE distributions of the water from which cement is precipitated and the particulate sediments themselves. Incorporation of particulate matter that scavenged REEs from the water column should: 1) increase ΣREE; 2) decrease LREE depletion (i.e., increase the $(Nd/Yb)_{sn}$ ratio); 3) decrease the La anomaly as particles scavenge less La relative to neighbouring REEs (Sholkovitz et al., 1994); and 4) decrease the Y/Ho ratio as particles scavenge little Y relative to Ho (Byrne and Lee, 1993). The effect on the Ce anomaly is more difficult to predict as it is also dependent on water depth among other parameters. Sholkovitz et al. (1994) noted that coatings that contained scavenged REEs in descending particles in the Sargasso Sea had negative Ce anomalies in the upper 100 m, but rapidly developed positive Ce anomalies below that depth. Hence, at the interpreted depths of the studied carbonate ramp, particulate matter raining down on the seafloor may have had LREE-enriched REE patterns with negative or positive Ce anomalies. Cross plots of $(La/La^*)_{sn}$ and Y/Ho versus ΣREE show that increasing ΣREEs are associated with rapidly declining but variable Y/Ho ratios and La anomalies in AL (Fig. 12). However, the individual AL values are highly variable and, although the Y/Ho ratio is reduced at a greater rate than would be expected from aeolian dust contamination, as predicted for incorporation of scavenging particles, only a weak correlation exists between ΣREE and Y/Ho ($R^2 = 0.4$), and there is no correlation between the La anomaly and REE concentration in AL samples. The mean values of AL normalised to RF as a local seawater proxy (Fig. 8b) show significant La and Y depletion as has been demonstrated in scavenging particles

(Sholkovitz et al., 1994). Hence, the data support the presence of a LREE-enriched source in AL that rapidly reduces the key anomalies as predicted by incorporation of LREE-scavenging particles. However, individual sample variability is consistent with multiple REE sources and processes that obscure exact relationships. Regardless, the data are not consistent with REEs representing solely incorporation of LREE-enriched aeolian dust or MuQ.

5.4. Microbialite categories MC1, MC2 and MC3: seawater-like vs. contaminated $(REE+Y)_{sn}$ patterns

The MC1 microbialite samples have similar $(REE+Y)_{sn}$ distributions to marine RF cement, but most of the other microbial carbonates (MC2 and MC3) have reduced LREE depletion and more variable anomalies (Figs. 5-7). The MC1 $(REE+Y)_{sn}$ distributions are similar to those of Upper Jurassic marine microbialites (Fig. 13) from the northern Tethys and eastern Atlantic margins (Olivier and Boyet, 2006), Permian marine carbonates of the Chichibu Terrane, Japan (Tanaka et al., 2003) and Devonian reefal microbialites in Western Australia (Nothdurft et al., 2004). The slightly lower LREE depletion relative to the RF cement (Fig. 8, 12) could suggest very minor incorporation of LREE-enriched particulate matter as in AL or enhanced LREE scavenging by organic matter in the microbial mat itself. The slightly reduced La anomaly (Fig. 7) and Y/Ho ratio (Fig. 11, 12) are consistent with both hypotheses. However, very low Zr, Th and Al_2O_3 contents (Fig. 10) suggest very limited trapping and binding of allochthonous sediment in MC1, which may favour a slight bias towards LREE uptake in the growing microbialite consistent with scavenging on organic ligands in the biofilm. Differences in REE distributions between microbialites and surrounding coeval particulate grainy sediments have been used to discriminate between microbial carbonate formation by trapping and binding or by *in situ* precipitation (Corkeron et al., 2012). In the present case, MC1 appears to represent microbial carbonate formed through *in situ* precipitation. The microbialites analysed by Corkeron et al. (2012) also had elevated LREEs relative to associated

carbonate grainstone, but there were no marine cements that could constrain the REE distribution of the water body in which they precipitated, and consequently any degree of initial LREE enrichment could not be calculated.

The fourteen MC2 samples have flatter patterns than the MC1 microbialites (Figs. 5-6), but their average REE concentration (ΣREE 5.27 ppm) is only slightly higher than MC1 samples (ΣREE 5.23), owing to the wide range of individual MC1 ΣREE values, some of which are much higher than some of the MC2 samples (Fig. 12a). The degree of LREE depletion, the Y/Ho ratio and the La and Ce anomalies are highly variable and do not correlate well with ΣREE for MC2 (Fig. 12), suggesting that the total REE concentrations reflect a variety of REE sources and/or processes. Most of the MC2 samples cannot be explained by any mixing line between RF cement or MC1 and MuQ or aeolian dust (Figs. 9, 11c-d, 12, 14), despite the correlation between the ΣREE versus the Zr and Th concentrations, which are similar to the values obtained by mixing RF and MC1 with MuQ clastics (Fig. 11a-b). The MC2 samples were probably not significantly contaminated by siliciclastic sediment (Fig. 14a), even though they show higher lithophile element and Al_2O_3 concentrations than RF (Fig. 11). MC2 samples lack correlation between increasing $(Nd/Yb)_{sn}$ and decreasing Y/Ho with increasing ΣREE as is displayed by the mixing curves of RF and MC1 with MuQ and aeolian dust (Fig. 12a-c). Hence, MC2 microbialites also appear to contain a source that added primarily LREE because their HREE concentrations are similar to those of mean marine RF cement. Mixing plots between MC1 microbialite and BS cement (Fig. 14b) or allomicrite (Fig. 14c) also do not trend towards the average values of MC2, because their $(REE+Y)_{sn}$ patterns seem to derive from RF marine cement values enriched in LREE rather than from MC1.

The seven leiolitic MC3 samples have $(REE+Y)_{sn}$ patterns more similar to allomicrite (Fig. 6) with total mean REE concentration (ΣREE = 9.96), higher than for MC1 and MC2, but with individual total concentrations less than the highest MC1 values (Figs. 11, 12). MC3 microbialites are less depleted in LREE than MC1, as for MC2 and AL (Figs. 11d, 12a), and have lower Y/Ho ratios versus ΣREE than MC2, AL and hypothetical mixing of RF and MC1 with MuQ and aeolian

dust (Fig. 11c, 12b-c). MC3 carbonates show the greatest enrichment in Al_2O_3 and siliciclastic derived trace elements such as Th and Zr, with concentrations even greater than in AL (Figs. 10, 11). To test fluvial siliciclastic contamination in the MC3 microbialites, their mean $(REE+Y)_{sn}$ concentrations were compared with theoretical mixing between RF cement and MuQ (Fig. 9b). This mixing model suggests that the leiolitic MC3 samples have $(LREE)_{sn}$ concentrations similar to the mixing between RF and 3-5% MuQ (Fig. 9b). Hypothetical mixing between mean MC1 and MuQ suggests that the MC3 samples have $(LREE)_{sn}$ concentrations close to those produced by mixing MC1 and 3% MuQ (Fig. 14a) but MC1 only reaches a flattened pattern with 10-20 % MuQ, which is not supported by lithophile element concentrations. Mixing plots between RF cement and MuQ and aeolian dust (Fig. 11, 12) highlight possible siliciclastic contamination for MC3 because of positive correlation between decreasing Y/Ho and flattening of the $(REE+Y)_{sn}$ (Fig. 12c). However, Al_2O_3, Zr and Th concentrations show that additional LREE-enriched sources are also required to produce the calculated higher $(Nd/Yb)_{sn}$ and lower Y/Ho ratios (Fig. 11c-d, 12a-c). Mixing plots between MC1 and BS cement (Fig. 14b) and allomicrite (Fig. 14c) do not trend towards the average values of MC3 as with MC2. The flattened patterns of MC3 are better approximated by mixing RF cement $(REE+Y)_{sn}$ with 3 % MuQ and 10 % burial cement, as with allomicrite (Fig. 15), but in both cases, the La anomaly is not reduced as much as would be expected with such a BS overprint. Regardless, a contribution from LREE enriched particles cannot be excluded because MC3 microbialites are enriched in LREE and depleted in HREE with respect to MC1, suggesting that their contamination with respect to the RF concentrations also might derive from a LREE-enriched source.

5.4.1. Ce anomaly in the microbialites

Despite the issues already discussed regarding the difficulty in quantifying small Ce anomalies, many of the analysed samples clearly have higher Ce concentrations than the interpreted

seawater source, based on RF cement. The variability of the Ce anomaly (including potentially small positive values) in the microbialites might be attributed partly to siliciclastic contamination, burial diagenesis in anoxic fluids, and incorporation of Ce-enriched particles that rained down from the water column as proposed for the allomicrites (e.g., Sholkovitz et al., 1994). Mean REE patterns normalised to the RF cement (Fig. 8b) suggest possible diagenetic or particulate input of Ce in AL, MC2 and MC3, but that was less significant in MC1. However, the Ce anomaly varied significantly in MC1 (Fig. 7, 12e-f), suggesting some initial or early diagenetic influence from anoxic/dysoxic fluids, potentially confined to localised microenvironments in some samples. The lack of correlation between increased $(Ce/Ce^*)_{sn}$ and decreasing LREE depletion for RF and MC1 is not consistent with significant direct incorporation of water column particles or with late overprint by BS cement (Fig. 12f). Hence, there also could have been an overprint from a subsequent anoxic early diagenetic fluid that has not provided an end-member cement in the analyzed samples. Haley et al. (2004) suggested that Ce is rapidly released into early marine burial suboxic pore fluids from oxide crusts on water column particles so as to reduce the negative Ce anomaly to unity. If Ce was enriched in early diagenetic fluids from adjacent sediments that contained abundant water column particles, then that could have reduced the negative Ce anomaly in the otherwise seawater-like MC1 samples without necessarily increasing the LREE concentration.

6. Discussion

The REE+Y distributions from upper Sinemurian sponge microbial mounds and surrounding skeletal coated grain packstone/grainstone, from middle to outer ramp settings of the DBD, exhibit different normalized REE patterns as a function of the sampled carbonate precipitate types (Figs. 5, 6). Early RF cements from stromatactis-like cavities within the mounds have typical seawater-like $(REE+Y)_{sn}$ signatures, although with variable Ce and La anomalies and Y/Ho ratios, confirming that the mounds accumulated in a well-oxygenated open marine setting. In addition, the

DBD data set is consistent with the Early Jurassic having had seawater REE distributions similar to those of modern seawater (cf. Shield and Webb, 2004; Olivier and Boyet, 2006).

6.1. Causes of spatially adjacent different (REE+Y)sn patterns

Microbially-mediated carbonates that form the bulk of the siliceous sponge mounds are in part good proxies for seawater $(REE+Y)_{sn}$ with higher REE concentrations than the RF cement as observed in other studies relative to recent and ancient microbialites (Fig. 13; Webb and Kamber, 2000; Nothdurft et al., 2004; Olivier and Boyet, 2006;Webb and Kamber, 2011). However, the REE+Y distributions of MC2 and MC3 microbialites differ from the RF cement and MC1. Microbial carbonates MC2 and MC3 deviate from the marine $(REE+Y)_{sn}$ pattern, tending to acquire a flattened pattern similar to the allomicrite (Fig. 4d, 5) with, in some cases, even higher concentrations of lithophile elements (Fig. 10), while occurring spatially adjacent to samples (MC1) that preserve a 'pristine' seawater signature. The less seawater-like $(REE+Y)_{sn}$ patterns of MC2 and MC3 microbialites and allomicrites appear to indicate various REE + Y sources, reflecting both sedimentary and diagenetic processes. These include: a) somewhat different initial uptake, b) terrigenous contamination of ~2-5 % terrestrial fines; c) a source of particulate contamination enriched in LREEs, with elevated Ce, that might reflect marine water column particles, although a component of LREE enriched aeolian dust is difficult to exclude from some samples; d) diagenetic fluids that were in contact with basinal siliciclastic deposits and or basalts underlying or overlying the carbonate succession or with Fe-Mn crusts forming hardgrounds in the succession (Merino Tome' et al., 2012); and possibly e) overprint from late hydrothermal fluids, which precipitated the saddle dolomite and idiomorphic quartz crystals and produced the MVT Pb-Zn mineralization higher in the stratigraphic succession.

With respect to terrigenous sediment contamination, Olivier and Boyet (2006) stressed for the Upper Jurassic Tethyan Pagney-sur-Meuse carbonates that microbialite REE+Y concentrations

can be altered by minimal clastic sediment input and that surrounding carbonate mud has higher terrigenous contamination than the microbial reefs. The deep shelf, sponge bioherm microbialites from Plettenberg, near Pagney-sur-Meuse on the northern Tethyan margin, have higher REE concentrations than the studied DBD MC1 carbonates (Olivier and Boyet, 2006; Fig. 13), with patterns similar to Upper Devonian reefal microbialites (Nothdurft et al., 2004), but lacking the superchondritic Y/Ho ratio typical of seawater. Their LREE enrichment, high ΣREE and low Y/Ho ratio, relative to the coeval clean Pagney-sur-Meuse deposits, are consistent with some contamination from terrigenous detritus (Olivier and Boyet, 2006). Regardless, MC1 carbonates in the DBD appear to preserve relatively undisturbed seawater REE distributions despite their close proximity to more 'contaminated' microbialites and late diagenetic pore occluding cements. Therefore, of the possible REE sources suggested, the incorporation of water column particles that scavenged REEs is particularly interesting as it may explain the difference in LREE content between seawater-like samples (RF and MC1) and the other microbial carbonates and allomicrite, which are comparatively LREE-enriched, but cannot be explained solely by typical fluvial or aeolian siliciclastic contamination or diagenetic overprint. A degree of LREE enrichment may also have occurred initially in the microbialites as organic ligands in the microbial biofilms preferentially scavenged LREEs from seawater, because the negative La anomaly and sub-unity Y/Ho ratio of MC1 normalised to RF cement (Fig 8b) is consistent with organic scavenging. However, that should not account for the differences between MC1 and MC2. The fine grained texture and associated microporosity of microbialite and allomicrite, and potential for trapping and binding for the microbialites and fall-out deposition for the allomicrite, render these carbonates more easily contaminated and/or altered than the marine cement. If LREE-enriched particulate materials from the water column were trapped and bound in seafloor sediments (coated grain skeletal packstone/wackestone) or into microbialites prior to the release of the REEs below the oxygen minimum zone, it could conceivably cause relative enrichment in LREEs in the absence of significant siliciclastic contamination. In this relatively clean carbonate setting, such particulate

material may be more abundant than siliciclastic fines and could accumulate below wave base thus affecting the REE distributions of allomicrite and microbialites that trapped and bound detrital material. Frimmel (2009) documented two types of $(REE+Y)_{sn}$ patterns in Neoproterozoic stromatolites, one type with LREE-depleted $(REE+Y)_{sn}$ patterns typical of shallow seawater and one type with relatively flat $(REE+Y)_{sn}$ patterns that reflected higher LREE concentrations. Frimmel (2009) interpreted the stromatolites with flat $(REE+Y)_{sn}$ patterns as having incorporated abundant fluvially-derived LREE-enriched organic colloids consistent with their position in continental fringing reefs. LREE-enriched, seawater-like $(REE+Y)_{sn}$ distributions were also identified in Devonian fringing reefs and were also attributed to incorporation of LREE-enriched colloids (Nothdurft et al., 2004). The potential for the DBD samples to have received fluvially derived colloids cannot be evaluated as the exact paleogeography of the Sinemurian rift valley is unknown, but Wilmsen and Neuweiler (2008) considered this time interval to have had a semi-arid climate with increasing overall bioproductivity through the late Sinemurian. Hence, moderately elevated lithophile element concentrations relative to more increased LREE concentrations in AL, MC2 and MC3 is consistent with incorporation of particles of marine origin that preferentially scavenged LREEs in the water column.

6.2. Bulk carbonate sampling: the role of sedimentary contamination and diagenetic alteration

The results from this study highlight the distinctive $(REE+Y)_{sn}$ signatures of different carbonate components and show that immediately adjacent carbonate types may have differing or variable REE concentrations that reflect different primary uptake and incorporation of various sedimentary sources. Additionally, different carbonate components were affected to differing degrees by burial diagenesis, rather than being 're-equilibrated' to the new fluids and homogenised in bulk. The patchy luminescence, which may represent burial neomorphism in MC3 carbonates in

particular, may be associated with their variable REE distributions, but their REE patterns do not trend into those of immediately adjacent RF cements, for example. These observations support the necessity of recognition and discrete sampling of the different carbonate components (e.g., through laser ablation or microdrilling) rather than bulk rock REE analysis. Otherwise the measured REE+Y concentrations are a combination of marine and diagenetically altered or contaminated carbonates. Himmler et al. (2010) stressed the importance of laser ablation spot sampling by demonstrating that $(REE+Y)_{sn}$ patterns in botryoidal aragonite precipitated in methane-seep carbonates vary even within the same cement crystal, from seawater-like to enriched in LREEs, because of evolving pore fluids during crystal growth. The significance of finely targeted vs. bulk rock sampling is emphasised by comparison of the present study with that of Wilmsen and Neuweiler (2008). Those authors applied REE+Y geochemistry to carbonate platform strata that are time-equivalent to the DBD, and with similar facies and vertical evolution, but developed on a different fault block in the High Atlas of Morocco. The whole rock $(REE+Y)_{sn}$ data displayed by Wilmsen and Neuweiler for the upper Sinemurian stage 2 siliceous sponge mounds show a bell shape typical of burial diagenesis (cf. Haley et al., 2004; Shields and Webb, 2004). Rachidi et al. (2009) interpreted similar MREE-enriched patterns in slightly younger Early Jurassic facies from the Middle Atlas of Morocco as reflecting burial diagenesis, but reported an associated belemnite sample that retained an original seawater-like $(REE+Y)_{sn}$ pattern.

6.3. Microbialites, oxygen minimum zone and Ce anomaly

Wilmsen and Neuweiler (2008) suggested that slightly negative Ce anomalies ($(Ce/Ce^*)_{sn}$ = 0.8) encountered in their bulk rock analyses might be indicative of either local recycling from dissolution of ferrous iron crusts or a pronounced oxygen minimum zone (OMZ). However, based on bulk rock REE analysis, the reduced Ce anomaly of Wilmsen and Neuweiler (2008) might represent early diagenetic Ce redistribution (e.g., Haley et al., 2004) or subsequent burial diagenesis

(e.g., BS cement from this study). Importantly, REE-scavenging marine particles in the water column may have carried increased Ce concentrations (i.e., with positive Ce anomaly) to the seafloor in the present study, thus allowing an additional source of elevated Ce without the need to invoke a shallow OMZ. Although equivocal in this study, as the Ce anomaly in scavenged particles at the depths of the studied ramp would be expected to be near unity (Sholkovitz et al., 1994), in deeper settings, such particles might provide the source for a significant positive Ce anomaly in sediment. Neuweiler et al. (2001) previously interpreted the Moroccan upper Sinemurian siliceous sponge mounds as having accumulated in association with an OMZ based on trophic structure within the sponge mounds, and Wilmsen and Neuweiler (2008) echoed that interpretation based on their REE data. However, this study, based on discrete sampling of carbonate precipitates of similar upper Sinemurian mounds from the DBD carbonate ramp, shows a prominent negative Ce anomaly for the early marine cement, indicating well-oxygenated seawater during mound growth. Similarly, Olivier and Boyet (2006) documented negative Ce anomalies in Upper Jurassic coral-microbialite and sponge microbial reefs from the northwestern Tethys and Eastern Atlantic shallow lagoon and deep shelf settings, respectively, ruling out dysoxic conditions for both. Hence, there is no requirement that abundant microbialite growth in Jurassic mounds was associated with anoxia within a shallow OMZ.

7. Conclusions

Upper Sinemurian siliceous sponge mounds that accumulated in middle to outer ramp settings in the High Atlas of Morocco (Djebel Bou Dahar, DBD) were analysed for trace elements at high spatial resolution on thin sections using laser ablation-inductively coupled plasma-mass spectrometry and powders were analysed separately by stable isotope mass spectrometry. The various carbonate components (e.g., marine radial/radiaxial fibrous cement - RF, burial blocky sparite cement - BS, allomicrite from skeletal coated grain packstone - AL, clotted peloidal and

leiolitic microbialite from siliceous sponge microbial mounds - MC1, MC2, MC3) yield important and consistent differences in the distributions of REE+Y despite very close proximity.

Burial diagenetic BS cement shows a distinct bell-shaped $(REE+Y)_{sn}$ pattern, whereas normal oxygenated seawater patterns (LREE depletion, positive La anomaly, negative Ce anomaly, high Y/Ho ratio) are preserved in RF cement and some microbialites (MC1), confirming that Early Jurassic seawater had a similar REE distribution to that observed today and apparently through the Phanerozoic. The microbial carbonates incorporated REEs at higher concentrations than marine RF cement and potentially with a small bias towards LREEs that would be consistent with initial complexation on organic ligands in the biofilm. Some microbialite samples (MC2, MC3) and allomicrite deviate from the marine REE+Y pattern, showing flattened, LREE enriched $(REE+Y)_{sn}$ patterns. These patterns appear to represent some incorporation of siliciclastic detrital sediment, but cannot be solely explained by addition of fluvial or aeolian sources. Their LREE enrichment may reflect incorporation of marine particulate organic matter that preferentially scavenged LREE from the water column. In addition, MC2 and MC3 microbialites and AL allomicrites may contain overprints from diagenetic fluids that were in contact with siliciclastic deposits, Fe-Mn crusts and/or hydrothermal sources. The siliceous sponge microbial mounds accumulated in well-oxygenated settings rather than in correspondence with an oxygen minimum zone as previously suggested (Neuweiler et al., 2001). Some of the elevated Ce concentrations of the microbialite samples may reflect redistribution of Ce during earliest diagenesis in suboxic pore fluids and/or sedimentary contamination by LREE-enriched particulate matter, which may have acquired a positive Ce anomaly below 100 m in the water column. If so, then a similar process could have implications for interpreting the redox state of ancient seawater.

The preservation of distinct seawater-like REE+Y distributions in comingled carbonate components in the same depositional environment rules out bulk re-equilibration of geochemistry during burial diagenesis and highlights the importance of analysing specific carbonate components,

which may reflect a variety of distinct and identifiable sedimentary sources and diagenetic processes, rather than whole rock samples, which provide homogenised data.

Acknowledgements

The stratigraphic and sedimentological framework of this study was developed in a project funded by Chevron ETC. Jeroen A.M. Kenter, Oscar Merino-Tomé, Juan Bahamonde, and Mitch Harris are thanked for stimulating discussions and contribution in the field. Julia Becker is warmly thanked for the stable isotope analyses at the School of Earth and Ocean Sciences, Cardiff University, UK. Reviewers J. Peckmann and B. Kamber, and Editor Michael Böttcher are warmly thanked for constructive improvements of the manuscript.

Appendix A. Supplementary online information

Supplementary data associated with this article can be found in the online version.

References

Adil, S., Bouabdellah, M., Grandia, F., Cardellach, E., Canals, A., 2004. Caractérisation géochimique des fluids associés aux minéralisations Pb-Zn de Bou-Dahar (Maroc). Comptes Rendus Geoscience 336, 1265-1272.

Alibo, D.S., Nozaki, Y., 1999. Rare earth elements in seawater: particle association, shale-normalization, and Ce oxidation. Geochimica et Cosmochimica Acta 63 (3-4), 363-372.

Alibo, D.S., Nozaki, Y., 2004. Dissolved rare earth elements in the eastern Indian Ocean: chemical tracers of the water masses. Deep-Sea Research I 51, 559-576.

Allwood, A.C., Kamber, B.S., Walter, M.R., Burch, I.W., Kanik, I., 2010. Trace elements record depositional history of an Early Archean stromatolitic carbonate platform. Chemical Geology 270, 148-163.

Andres, M.S, Sumner, D.Y., Reid, R.P., 2006. Isotopic fingerprints of microbial respiration in aragonite for Bahamian stromatolites. Geology 34, 973-976.

Azmy, K., Brand, U., Sylvester, P., Gleeson, S.A., Logan, A., Bitner, M.A., 2011. Biogenic and abiogenic low-Mg calcite (bLMC and aLMC): evaluation of seawater-REE composition, water masses and carbonate diagenesis. Chemical Geology 280, 180-190.

Banner, J.L., Hanson, G.N., Meyers, W.J., 1988. Rare earth element and Nd isotopic variations in regionally extensive dolomites from the Burlington-Keokuk Formation (Mississippian): Implications for REE mobility during carbonate diagenesis. Journal of Sedimentary Petrology 58, 415-432.

Banner, J.L., Hanson, G.N., 1990. Calculation of simultaneous isotopic and trace element variations during water-rock interaction with applications to carbonate diagenesis. Geochimica et Cosmochimica Acta 54, 3123-3137.

Barrat, J.A., Boulegue, J., Tiercelin, J.J., Lesourd, M., 2000. Strontium isotopes and rare-earth element geochemistry of hydrothermal carbonate deposits from Lake Tanganyika, East Africa. Geochimica et Cosmochimica Acta, 64, 287-298.

Bau, M., 1996. Controls on the fractionation of isovalent trace elements in magmatic and aqueous systems: evidence from Y/Ho, Zr/Hf, and lanthanide tetrad effect. Contributions to Mineralogy and Petrology 123, 323-333.

Bau, M., Möller, P., 1993. Rare earth element systematic of the chemically precipitated component in early Precambrian iron formations and the evolution of the terrestrial atmosphere-hydrosphere-lithosphere system. Geochimica et Cosmochimica Acta 57, 2239-2249.

Bolhar, R., Van Kranendonk, M.J., 2007. A non-marine depositional setting for the northern Fortescue Group, Pilbara Craton, inferred from trace element geochemistry of stromatolitic carbonates. Precambrian Research 155, 229-250.

Bolhar R., Kamber B. S., Moorbath S., Fedo C. M., Whitehouse M. J., 2004. Characterization of early Archaean chemical sediments by trace element signatures. Earth and Planetary Science Letters 222, 43–60.

Burne, R.V., Moore, L.S., 1987. Microbialites: organosedimentary deposits of benthic microbial communities. Palaios 2, 241–254.

Byrne, R.H., Kim, K.-H., 1990. Rare earth element scavenging in seawater. Geochimica et Cosmochimica Acta 54, 2645-2656.

Byrne, R.H., Lee, J.H., 1993. Comparative yttrium and rare earth element chemistries in seawater. Marine Chemistry 44, 121-130.

Cabioch, G., Camoin, G.F., Webb, G.E., Le Cornec, F., Molina, M.G., Pierre, C., Joachimski, M.M., 2006. Contribution of microbialites to the development of coral reefs during the last deglacial period: case study from Vanuatu (South-West Pacific). Sedimentary Geology 185, 297-318.

Camoin, G.F., Gautret, P., Montaggioni, L.F., Cabioch, G., 1999. Nature and environmental significance of microbialites in Quaternary reefs: the Tahiti paradox. Sedimentary Geology 126, 271-304.

Corkeron, M., Webb, G.E., Moulds, J., Grey, K. 2012. Discriminating stromatolite formation modes using rare earth element geochemistry: trapping and binding versus in situ precipitation of stromatolites from the Neoproterozoic Bitter Springs Formation, Northern Territory, Australia. Precambrian Research 212-213, 194-206.

Della Porta G., Merino-Tomé O., Kenter J.A.M., Verwer K., 2013. Lower Jurassic microbial and skeletal carbonate factories and platform geometry (Djebel Bou Dahar, High Atlas, Morocco). In: Verwer, K., Playton, T.E., Harris, P.M. (Eds.), Deposits, architecture, and

controls of carbonate margin, slope, and basinal settings. SEPM (Society for Sedimentary Geology) Special Publication 105, 237-263, Tulsa, OK. doi: 10.2110/sepmsp.105.01.

Derry L.A., Jacobsen S.B., 1990. The chemical evolution of Precambrian seawater: evidence from REEs in banded iron formations. Geochimica et Cosmochimica Acta 54, 2965–2977.

Di Leonardo, R., Bellanca, A., Neri, R., Tranchida, G., Mazzola, S., 2009. Distribution of REEs in box-core sediments offshore an industrial area in SE Sicily, Ionian Sea: evidence of anomalous sedimentary inputs. Chemosphere 77, 778-784.

Elderfield, H., 1988. The oceanic chemistry of the rare-earth elements. Philosophical Transactions Royal Society London 325**,** 105–106.

Elderfield, H., Greaves, M.J., 1982. The rare earth elements in seawater. Nature 296, 214-219.

Elderfield, H., Upstill-Goddard, R., Sholkovitz, E.R., 1990. The rare earth elements in rivers, estuaries, and coastal seas and their significance to the composition of ocean waters. Geochimica et Cosmochimica Acta 54, 971-991.

Frei, R., Polat, A., 2007. Source heterogeneity for the major components of ~ 3.7 Ga Banded Iron Formations (Isua Greenstone Belt, Western Greenland): tracing the nature of interacting water masses in BIF formation. Earth and Planetary Science Letters 253, 266-281.

Frimmel, H.E., 2009. Trace element distribution in Neoproterozoic carbonates as palaeoenvironmental indicator. Chemical Geology 258, 338-353.

German, C.R., Elderfield, H., 1990. Application of Ce anomaly as a paleoredox indicator: the ground rules. Paleoceanography 5, 823-833.

Grandjean-Lécuyer, P., Feist, R., Albarede, F., 1993. Rare earth elements in old biogenic apatites. Geochimica et Cosmochimica Acta 57, 2507-2514.

Greaves, M.J., Elderfield, H., Sholkovitz, E.R., 1999. Aeolian sources of rare earth elements to the Western Pacific Ocean. Marine Chemistry 68, 31–38.

Guido, A., Mastandrea, A., Tosti, F., Russo, F., 2011. Importance of rare earth element patterns in discriminating between biotic and abiotic mineralization, in: Reitner, J., Quéric, N.-V., Arp, G. (Eds.), Advances in Stromatolite Geobiology. Springer, Berlin, pp. 433-442.

Guido, A., Mastandrea, A., Rosso, A., Sanfilippo, R., Tosti, F., Riding, R., Russo, F., 2014. Commensal symbiosis between agglutinated polychaetes and sulfate-reducing bacteria. Geobiology, 12, 265-275.

Haley, B.A., Klinkhammer, G.P., McManus, J., 2004. Rare earth elements in pore waters of marine sediments. Geochimica et Cosmochimica Acta 68, 1265-1279.

Heindel, K., Birgel, D., Peckmann, J., Kuhnert, H., Westphal, H., 2010. Formation of deglacial microbialites in coral reefs off Tahiti (IODP 310) involving sulphate-reducing bacteria. Palaios 25, 618-635.

Himmler, T., Bach, W., Bohrmann, G., Peckmann, J. 2010. Rare earth elements in authigenic methane-seep carbonates as tracers for fluid composition during early diagenesis. Chemical Geology 277, 126–136.

Holser, W.T., 1997. Evaluation of the application of rare-earth elements to paleoceanography. Palaeogeography, Palaeoclimatology, Palaeoecology, 132, 309-323.

Hongo, Y., Obata, H., Alibo, D.S., Nozaki, Y., 2006. Spatial variations of Rare Earth Elements in North Pacific surface water. Journal of Oceanography 62, 441-455.

Kamber B.S., 2010. Archean mafic–ultramafic volcanic landmasses and their effect on ocean–atmosphere chemistry. Chemical Geology 274, 19-28.

Kamber, B.S., Bolhar, R., Webb, G.E., 2004. Geochemistry of late Archaean stromatolites from Zimbabwe: evidence for microbial life in restricted epicontinental seas. Precambrian Research 132, 379-399.

Kamber, B.S., Greig, A., Collerson, K.D., 2005. A new estimate for the composition of weathered young upper continental crust from alluvial sediments, Queensland, Australia, Geochimica et Cosmochimica Acta 69, 1041-1058.

Kamber, B.S., Webb, G.E., 2001. The geochemistry of late Archaean microbial carbonate: implications for ocean chemistry and continental erosion history. Geochimica et Cosmochimica Acta 65, 2509-2525.

Kamber, B.S., Webb, G.E., Gallagher, M., 2014. The rare earth element signal in Archaean microbial carbonate: information on ocean redox and biogenicity. Journal of the Geological Society, 171/6, 745-763.

Keupp, H., Jenisch, A., Herrmann, R., Neuweiler, F., Reitner, J., 1993. Microbial carbonate crusts – a key to the environmental analysis of fossil spongiolites?. Facies 29, 41-54.

Lawrence, M.G., Greig, A., Collerson, K.D., Kamber, B.S., 2006. Rare earth element and yttrium variability in southeast Queensland waterways. Aquatic Geochemistry 12, 39-72.

Lécuyer, C., Reynard, B., Grandjean, P., 2004, Rare earth element evolution of Phanerozoic seawater recorded in biogenic apatites. Chemical Geology 204, 63-102.

Londry, K.L., Des Marais, D.J., 2003. Stable carbon isotope fractionation by sulphate reducing bacteria. Applied and Environmental Microbiology 69, 2942-2949.

Luo Y.-R., Byrne, R.H., 2004. Carbonate complexation of Yttrium and the Rare Earth Elements in Natural Waters. Geochimica et Cosmochimica Acta 68, 691-699.

Marx, S.K., Kamber, B.S., McGowan, H.A., 2005. Provenance of long-travelled dust determined with ultra-trace-element composition: a pilot study with samples from New Zealand glaciers. Earth Surface Processes and Landforms 30, 699–716.

Marzoli, A., Bertrand, H., Knight, K.B., Cirilli, S., Buratti, N., Verati, C.l., Nomade, S.b., Renne, P.R., Youbi, N., Martini, R., Allenbach, K., Neuwerth, R., Rapaille, C.D., Zaninetti, L., Bellieni, G., 2004. Synchrony of the Central Atlantic magmatic province and the Triassic–Jurassic boundary climatic and biotic crisis. Geology 32, 973–976.

McLennan S.M., 1989 Rare earth elements in sedimentary rocks: influence of provenance and sedimentary processes. Reviews in Mineralogy 11, 169-200.

Merino-Tomé, O., Della Porta, G., Kenter, J.A.M., Verwer, K., Harris, P.M., Adams, E., Playton, T., Corrochano, D., 2012. Sequence development in an isolated carbonate platform (Lower Jurassic, Djebel Bou Dahar, High Atlas, Morocco): influence of tectonics, eustacy and carbonate production. Sedimentology 59, 118-155.

Neuweiler, F., Gautret, P., Thiel, V., Langes, R., Michaelis, W., Reitner, J. 1999. Petrology of Lower Cretaceous carbonate mud mounds (Albian, N. Spain): insights into organomineralic deposits of the geological record. Sedimentology, 46, 837-859.

Neuweiler, F., Mehdi, M., Wilmsen, M. 2001. Facies of Liassic sponge mounds, Central High Atlas, Morocco. Facies 243-264.

Nothdurft, L.D., Webb, G.E., Kamber, B.S., 2004. Rare earth element geochemistry of Late Devonian reefal carbonates, Canning Basin, Western Australia: confirmation of a seawater REE proxy in ancient limestones. Geochimica et Cosmochimica Acta 68, 263-283.

Nozaki, Y., Zhang, J., Amakawa, H., 1997. The fractionation between Y and Ho in the marine environment. Earth and Planetary Science Letters 148, 329-340.

Nozaki, Y., Alibo, D.S., 2003a. Dissolved rare earth elements in the Southern Ocean, southwest of Australia: unique patterns compared to South Atlantic data. Geochemical Journal 37, 47-62.

Nozaki, Y., Alibo, D.S., 2003b. Importance of vertical geochemical processes in controlling the oceanic profiles of dissolved rare earth elements in northeastern Indian Ocean, Earth and Planetary Science Letters 205, 155-172.

Olivier, N, Boyet M., 2006. Rare earth and trace elements of microbialites in Upper Jurassic coral- and sponge-microbialite reefs. Chemical Geology 230, 105-123.

Picard, S., Lécuyer, C., Barrat, J.-A., Garcia, J.-P., Dromart, G., Sheppard, S.M.F., 2002. Rare earth element contents of Jurassic fish and reptile teeth and their potential relation to seawater composition (Anglo-Paris Basin, France and England). Chemical Geology 186, 1-16.

Rachidi, M., Neuweiler, F., Kirkwood, D., 2009. Diagenetic-geochemical patterns and fluid evolution history of a Lower Jurassic petroleum source rock, Middle Atlas, Morocco. Journal of Petroleum Geology 32, 111-128.

Railsback, L.B., Hood, E.C. 2001. A survey of multi-stage diagenesis and dolomitization of Jurassic limestones along a regional shelf-to-basin transect in the Ziz Valley, Central High Atlas Mountains, Morocco. Sedimentary Geology 139, 285–317.

Reitner, J. 1993. Modern cryptic microbialite/metazoan facies from Lizard Island (Great Barrier Reef, Australia) - formation and concept. Facies, 29, 3-40.

Reitner, J., Neuweiler, F., Gautret, P., 1995. Modern and fossil automicrites: implications for mud mound genesis, in: Reitner, J., Neuweiler, F., coords., A polygenetic spectrum of fine-grained carbonate buildups. Facies 32, 4-17.

Reynard, B., Lécuyer, C., Grandjean, P., 1999. Crystal-chemical controls on rare-earth element concentrations in fossil biogenic apatites and implications for paleoenvironmental reconstructions. Chemical Geology 155, 233-241.

Rosales, I., Quesada, S., Robles, S., 2001. Primary and diagenetic isotopic signals in fossils and hemipelagic carbonates: the Lower Jurassic of northern Spain. Sedimentology 48, 1149-1169.

Shields, G.A., Webb, G.E., 2004. Has the REE composition of seawater changed over geological time? Chemical Geology 204, 103-107.

Sholkovitz, E.R., Landing, W.M., Lewis, B.L., 1994. Ocean particle chemistry: the fractionation of rare earth elements between suspended particles and seawater. Geochimica et Cosmochimica Acta 58, 1567-1579.

Tachikawa, K., Jeandel, C., Vangriesheim, A., Dupré, B., 1999. Distribution of rare earth elements and neodymium isotopes in suspended particles of the tropical Atlantic Ocean (EUMELI site). Deep-Sea Research I 46, 733-755.

Tang, Y., Han, G., Wu, Q., Xu, Z., 2013. Use of rare earth element patterns to trace the provenance of the atmospheric dust near Beijing, China. Environmental Earth Science 68, 871-879.

Tanaka, K., Miura, N., Asahara, Y., Kawabe, I. 2003. Rare earth element and strontium isotope study of seamount-type limestones in Mesozoic accretionary complex of Southern Chichibu Terrane, central Japan: Implications for incorporation process of seawater REE into limestones. Geochemical Journal 37, 163-180.

Tanaka, K., Kawabe, I. 2006. REE abundances in ancient seawater inferred from marine limestone and experimental REE partition coefficients between calcite and aqueous solution. Geochemical Journal 40, 425–435.

Teixell, A., Arboleya, M.-L., Julivert, M., 2003. Tectonic shortening and topography in the central High Atlas (Morocco). Tectonics 22, 1051.

Terakado, Y., Masuda, A. 1988. The coprecipitation of rare-earth elements with calcite and aragonite. Chemical Geology 69, 103–110.

Van Kranendonk, M.J., Webb, G.E., Kamber, B.S., 2003. Geological and trace element evidence for a marine sedimentary environment of deposition and biogenicity of 3.45 Ga stromatolitic carbonates in the Pilbara Craton, and support for a reducing Archean ocean. Geobiology 1, 91-108.

Veizer, J., Ala, D., Azmy, K., Bruckschen, P., Buhl, D., Bruhn, F., Garden, G.A.F., Diener, A., Ebneth, S., Godderis, Y., Jasper, T., Korte, C., Pawellek, F., Podlaha, O.G., Strauss, H., 1999. $^{87}Sr/^{86}Sr$, $\delta^{13}C$ and $\delta^{18}O$ evolution of Phanerozoic water. Chemical Geology 161, 59-88.

Verwer, K., Della Porta, G., Merino-Tome' O., Kenter, J.A.M., 2009a Controls and predictability of carbonate facies architecture in a Lower Jurassic three-dimensional barrier-shoal complex (Djebel Bou Dahar, High Atlas, Morocco). Sedimentology 56, 1801-1831.

Verwer, K., Merino-Tomé, O., Kenter, J.A.M., Della Porta, G., 2009b. Evolution of a high-relief carbonate platform slope using 3D digital outcrop models: lower Jurassic Djebel Bou Dahar, High Atlas, Morocco. Journal of Sedimentary Research 79, 416-439.

Webb, G.E., 1999. Youngest Early Carboniferous (late Visean) shallow-water patch reefs in eastern Australia (Rockhampton Group, Queensland): combining quantitative micro- and macro-scale data. Facies 41, 111-140.

Webb, G.E., Kamber, B.S., 2000. Rare earth elements in Holocene reefal microbialites: a new shallow seawater proxy. Geochimica et Cosmochimica Acta 64, 1557-1565.

Webb, G.E., Kamber, B.S., 2011. Trace element geochemistry as a tool for interpreting microbialites, in: Golding, S.D., Glikson, M. (Eds.), Earliest Life on Earth: Habitats, Environments and Methods of Detection. Springer, Dordrecht, pp. 127-170.

Webb, G.E., Baker, J.C., Jell, J.S. 1998. Inferred syngenetic textural evolution in Holocene cryptic reefal microbialites, Heron Reef, Great Barrier Reef, Australia. Geology, 26, 355-358.

Webb, G.E., Nothdurft, L.D., Kamber, B.S., Kloprogge, J.T., Zhao, J.-X., 2009. Rare earth element geochemistry of scleractinian coral skeleton during meteoric diagenesis: a sequence through neomorphism of aragonite to calcite. Sedimentology 56, 1433-1463.

Webb, G.E., Nothdurft L.D., Kamber B.S., 2012. Reply to Comment on "Rare earth element geochemistry of scleractinian coral skeleton during meteoric diagenesis: a sequence through neomorphism of aragonite to calcite" by Webb et al., Sedimentology 56, 1433-1463. Sedimentology 59, 733-736.

Wilmsen, M., Neuweiler, F., 2008. Biosedimentology of the Early Jurassic post-extinction carbonate depositional system, central High Atlas rift basin, Morocco. Sedimentology 55, 773-807.

Zhang, J., Nozaki, Y., 1996. Rare earth elements and yttrium in seawater: ICP-MS determinations in the East Caroline, Coral Sea, and South Fiji basins of the western South Pacific Ocean. Geochimica et Cosmochimica Acta 60, 4631- 4644.

Zhang, J., Nozaki, Y., 1998. Behavior of rare earth elements in seawater at the ocean margin: a study along the slopes of the Sagami and Nankai troughs near Japan. Geochimica et Cosmochimica Acta 62, 1307–1317.

Zhong, S., Mucci, A. 1995. Partitioning of rare earth elements (REEs) between calcite and seawater solutions at 25°C and 1 atm, and high dissolved REE concentrations. Geochimica et Cosmochimica Acta 59, 443–453.

Table and Figure captions

Table 1: Mean values of oxygen and carbon stable isotope measurements of the distinguished carbonate precipitate categories. Complete data set is provided in Supplementary Online Information Table 1.

Table 2: Mean values of the REE+Y and some trace element concentrations and calculated parameters of the distinguished carbonate precipitate categories.

Figure 1: a) Present-day location of the Djebel Bou Dahar (DBD) carbonate platform in the High Atlas of Morocco. b) Cross section drawn at the time of deposition of sequence III (late Sinemurian p.p.) showing the lateral distribution of siliceous sponge microbial mounds from South to North across the DBD carbonate platform (modified after Merino-Tomé et al., 2012; Della Porta et al., 2013). Mounds accreted in settings below effective wave base in the middle to outer ramp belts (southern margin) and in the deeper portion of the slope on the northern margin. CAMP refers to the Central Atlantic Magmatic Province basalts (cf. Marzoli et al., 2004).

Figure 2: a) Outcrop photo showing a siliceous sponge microbial mound overlain by decimetre-thick bedded coated grain skeletal packstone. The grey continuous line marks the base of the mound and the black dashed line shows the mound top (modified after Della Porta et al., 2013). b) Coated grain (C) skeletal packstone with allomicrite sediment matrix (AL) and foraminifera such as *Lenticulina* (L) and *Involutina liassica* (I). c) Mound microbial framework with a hexactinellid sponge body (H) at the base and on the left side within clotted peloidal micrite (MC1) overlain by leiolitic (structureless) microbialite (MC2) and sparse sponge spicules (S). d) Close-up view of a hexactinellid sponge (H), clotted peloidal micrite and tubes of the agglutinating worm *Terebella* (T). e) Stromatactis-like cavities with irregular tops and flat base filled by radiaxial fibrous cement

(RF) and occluded by blocky sparite (BS) within leiolitic microbialite (MC) with sparse siliceous sponge spicules (S), *Terebella* (T) and peloids. f) Thin section stained with alizarine red and potassium ferricyanide showing a primary cavity supported by clotted peloidal micrite (MC1) and laminated (MC2) microbialite filled by radiaxial fibrous cement (RF) with pink stained prismatic overgrowth followed by blue stained burial blocky sparite cement (BS) atop an internal sediment (IS)..

Figure 3: Plot of stable O and C isotope ratios of the carbonate categories composing the siliceous sponge microbial mounds and surrounding coated grain skeletal packstone/grainstone. Note that the RF radial/radiaxial fibrous cement, brachiopods and microbialites plot near each other, well within the field for normal Early Jurassic marine values.

Figure 4: Examples of discrete sampling on thin sections and the corresponding plots of $(REE+Y)_{sn}$ patterns. a) Photomicrograph of the sampling spots in thin section SP3 12.8: spot 1 corresponds to radial/radiaxial fibrous (RF) cement; spot 2 to blocky sparite (BS) cement; spot 3 corresponds to RF cement as in 1. b) Close-up view of sampling spot 2 with blocky sparite (BS) cement. c) Plot of the $(REE+Y)_{sn}$ patterns of the three sampling spots of thin section SP3 12.8. The RF cement sampled in two different spots shows a similar LREE depleted pattern contrasting with the bell-shaped pattern recorded by the BS cement. d) Plot of the $(REE+Y)_{sn}$ patterns of the five sampling spots of thin section SP3 2.8, shown in Figures 4e-g, highlighting the different patterns of blocky sparite (BS) cement, radial/radiaxial fibrous (RF) cement and microbialite types MC1 clotted peloidal micrite and MC3 leiolitic micrite (. Note that MC1 has a similar REE distribution to the RF cement, while MC3 shows a relatively flat $(REE)_{sn}$ pattern. e) Detail of MC3 leiolitic microbialite with sparse sponge spicules sampled in spot 4 of Figure 4g. f-g) Spots sampled in thin section SP3-2.8 with $(REE+Y)_{sn}$ patterns shown in Figure 4d: spot 1 corresponds to RF cement (two measurements in the same spot giving the same pattern); spot 2 corresponds to the MC1 clotted peloidal micrite shown

in 4d with the same pattern as RF cement; spot 3 corresponds to the bell-shaped pattern of the BS cement; spot 4 is the leiolitic microbialite MC3 shown in Figure 4e.

Figure 5: Plots of the $(REE+Y)_{sn}$ distributions of the six distinguished carbonate components: RF – radial/radiaxial fibrous cement, BS – blocky sparite, AL - allomicrite, microbialite types MC1, MC2 and MC3.

Figure 6: Plot of the mean $(REE+Y)_{sn}$ values of the six distinguished carbonate components (RF – radial/radiaxial fibrous cement, BS – blocky sparite cement, AL allomicrite, microbialite types MC1, MC2 and MC3) and burial saddle dolomite.

Figure 7: Plots of the Ce versus La anomalies of the six major carbonate components. Note that the radial/radiaxial fibrous (RF) cements and MC1 microbialite occur near each other relative to all other categories.

Figure 8: a) Distribution coefficients for REE+Y between radial/radiaxial fibrous (RF) cement and microbialites MC1 and modern seawater from the upper 200 m and 50 m in the South Pacific Ocean (data after Zhang and Nozaki, 1996). Distribution coefficients are calculated as D_{REE} = [REE proxy/REE seawater] * [Ca seawater/ Ca proxy], where [Ca seawater] is 0.01 mol/kg and [Ca proxy] is 10 mol/kg. b) REE+Y distributions relative to RF cement (as a proxy for Early Jurassic seawater in the High Atlas of Morocco). Note that the MC1 microbialite has an elevated, but relatively flat pattern compared to RF cement, whereas most of the other patterns are significantly LREE enriched. The decreased La and Y enrichment suggests that differences in complexation behaviour play a role in the REE uptake as La and Y are scavenged at a lower rate than similar REEs, such as Ho, with respect to carbonate and organic ligands (Nozaki et al., 1997). The BS cement has the highest LREE enrichment with increased Gd and Eu.

Figure 9: Plots of the $(REE+Y)_{sn}$ concentrations determined through hypothetical mixing between marine radial/radiaxial fibrous (RF) cement, MuQ and blocky sparite (BS) cement $(REE+Y)_{sn}$ concentrations compared with the measured mean values of the six main carbonate categories.

Figure 10: a) Cross plot of measured values of Th and Al_2O_3 content. Microbialite MC1 plots near the two cement types (RF radial fibrous and BS blocky sparite cement), whereas MC2 microbialites, allomicrite AL and microbialites MC3 plot with increasingly higher values. b) Cross plot of measured values of Zr and Al_2O_3 content. MC1 plots near the two cement types, whereas MC2, AL, and MC3 plot with increasingly higher values. c) Cross plot of measured values of Th and Zr content. MC2, AL and MC3 plot with increasingly higher values. MC1 microbialites are enriched in Th with respect to RF and BS cements.

Figure 11: a) Cross plot of ΣREE and Zr content and calculated mixing between radial/radiaxial fibrous (RF) cement and MC1 microbialites with MuQ terrigenous sediment and with the most LREE-enriched aeolian dust concentration (Buccleuch sample) of Marx et al. (2005). Note that MC2 and MC3 plot close to the mixing lines but allomicrite AL shows higher ΣREE concentrations at low Zr values than hypothetical mixing with dust or MuQ. b) Cross plot of ΣREE and Th content with similar trends to Zr content. c) Cross plot of Y/Ho and Al_2O_3 content. Note that MC2, AL, and MC3 plot with successively lower, but still superchondritic values mostly well below the mixing lines. d) Cross plot of $(Nd/Yb)_{sn}$ and Th content. Note that most AL, MC2, and MC3 samples show much less LREE depletion (i.e., higher $(Nd/Yb)_{sn}$) with increasing Th, than would be consistent with hypothetical mixing lines for dust or MuQ, thus suggesting an additional source of LREEs.

Figure 12: Plots comparing LREE depletion $(Nd/Yb)_{sn}$, Y/Ho, ΣREE, Ce and La anomalies for the distinguished carbonate categories (RF – radial/radiaxial fibrous cement, AL allomicrite,

microbialite types MC1, MC2 and MC) and calculated mixing between radial/radiaxial fibrous (RF) cement and MC1 microbialites with MuQ terrigenous sediment and with aeolian dust (Buccleuch sample, Marx et al. 2005). Note MC2, MC3 and AL generally do not trend along MuQ or aeolian dust mixing lines.

Figure 13: MuQ normalised REE+Y patterns of the Djebel Bou Dahar (DBD) Lower Jurassic mound mean MC1 microbialites compared with microbialites of Late Devonian (Leonard Shelf, Australia, Nothdurft et al., 2004), Permian (Ishimaki Limestone, Chichibu Terrane, Japan, Tanaka et al., 2003), Upper Jurassic deep shelf sponge mounds (Plettenberg, Olivier and Boyet, 2006), Upper Jurassic pure carbonate lagoon (Pagney-sur-Meuse, Olivier and Boyet, 2006), and Holocene microbialites (Great Barrier Reef; Webb and Kamber 2000).

Figure 14: Plots of the $(REE+Y)_{sn}$ concentrations determined through hypothetical mixing between pristine microbialite MC1, MuQ, blocky sparite (BS) cement and allomicrite (AL) $(REE+Y)_{sn}$ concentrations compared with the measured mean values of the six main carbonate categories. Note that hypothetical mixing with MuQ and BS cement does not produce distributions similar to microbialites types MC2 and MC3 or AL allomicrite and that mixing of AL and radial/radiaxial fibrous (RF) cement does not produce distributions similar to MC2 and MC3 microbialites.

Figure 15: Plot of the mean $(REE+Y)_{sn}$ concentrations compared with the hypothetical mixing of radial/radiaxial fibrous (RF) cement values with a few percentages of MuQ terrigenous sediment and blocky sparite (BS) cement. Note that MC3 microbialites falls between the two hypothetical mixed values and AL allomicrite almost coincides with 85.5 % RF + 4.5 % MuQ and 10% BS.

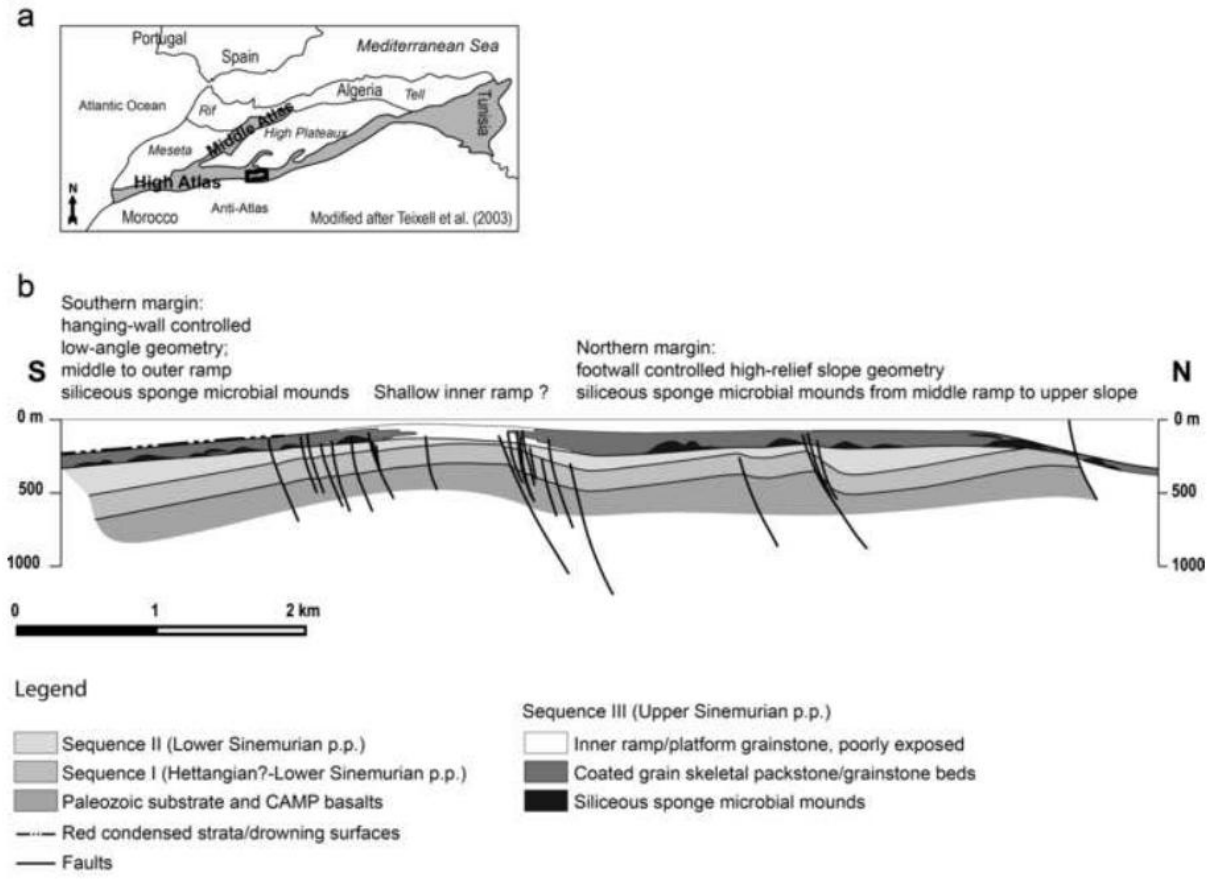

Figure 1

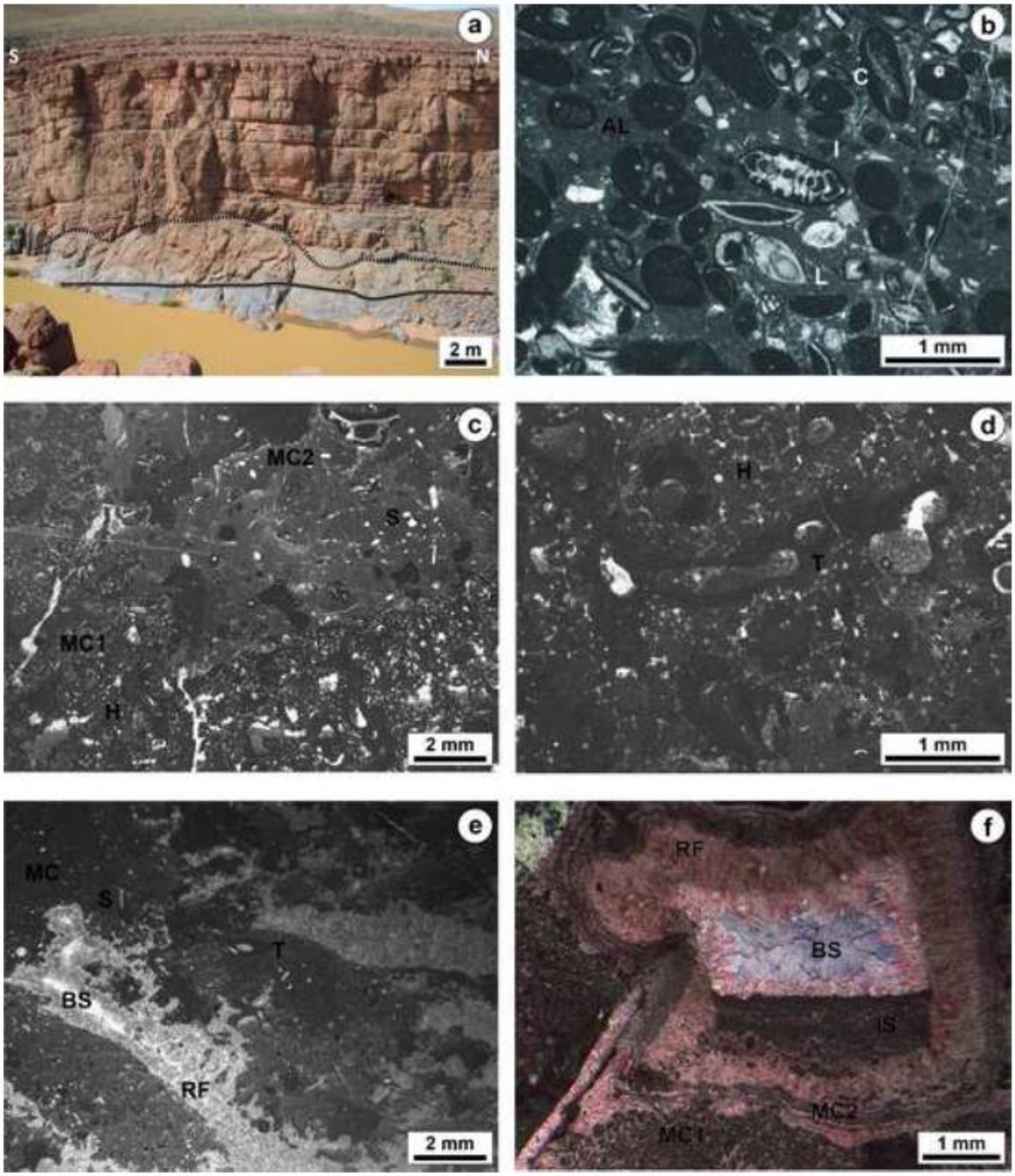

Figure 2

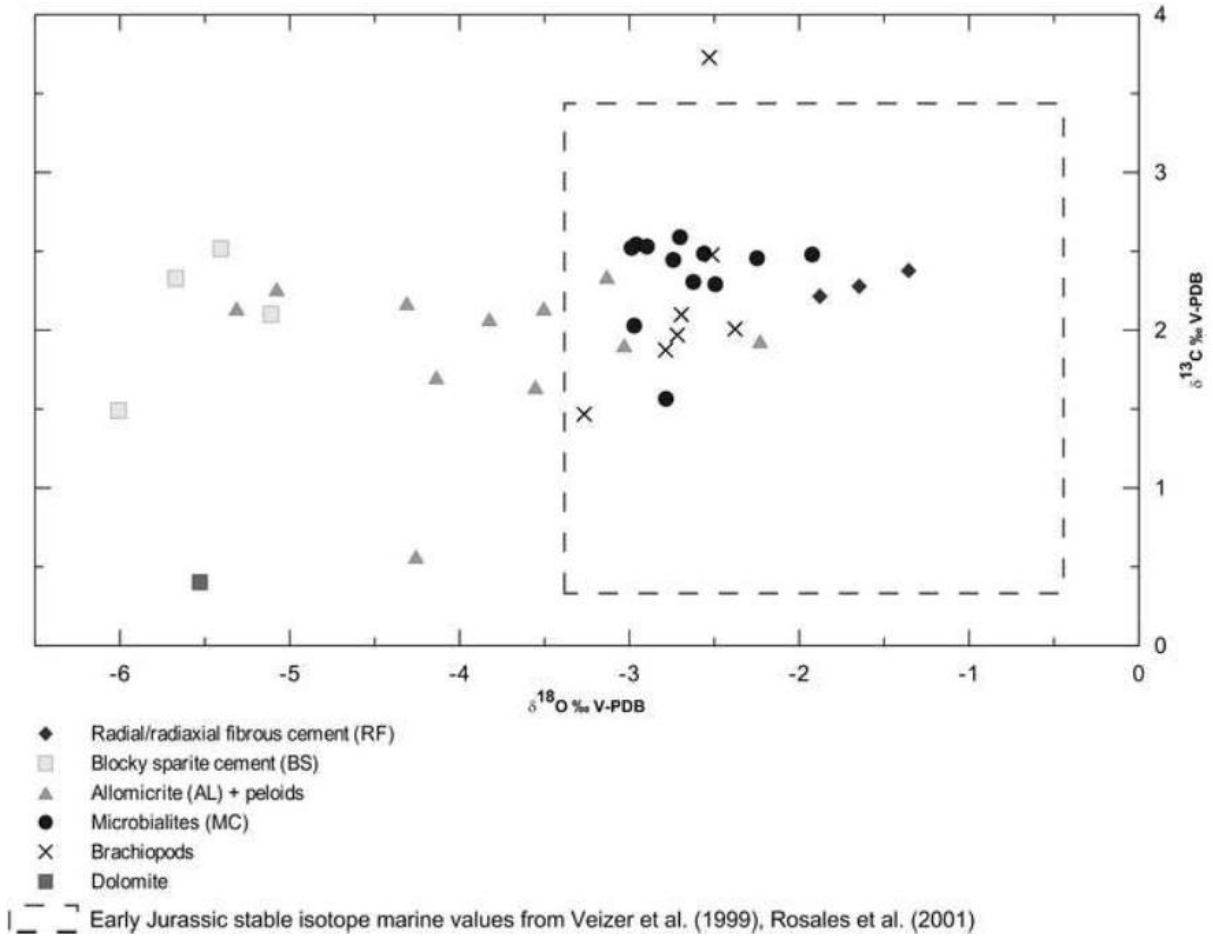

Figure 3

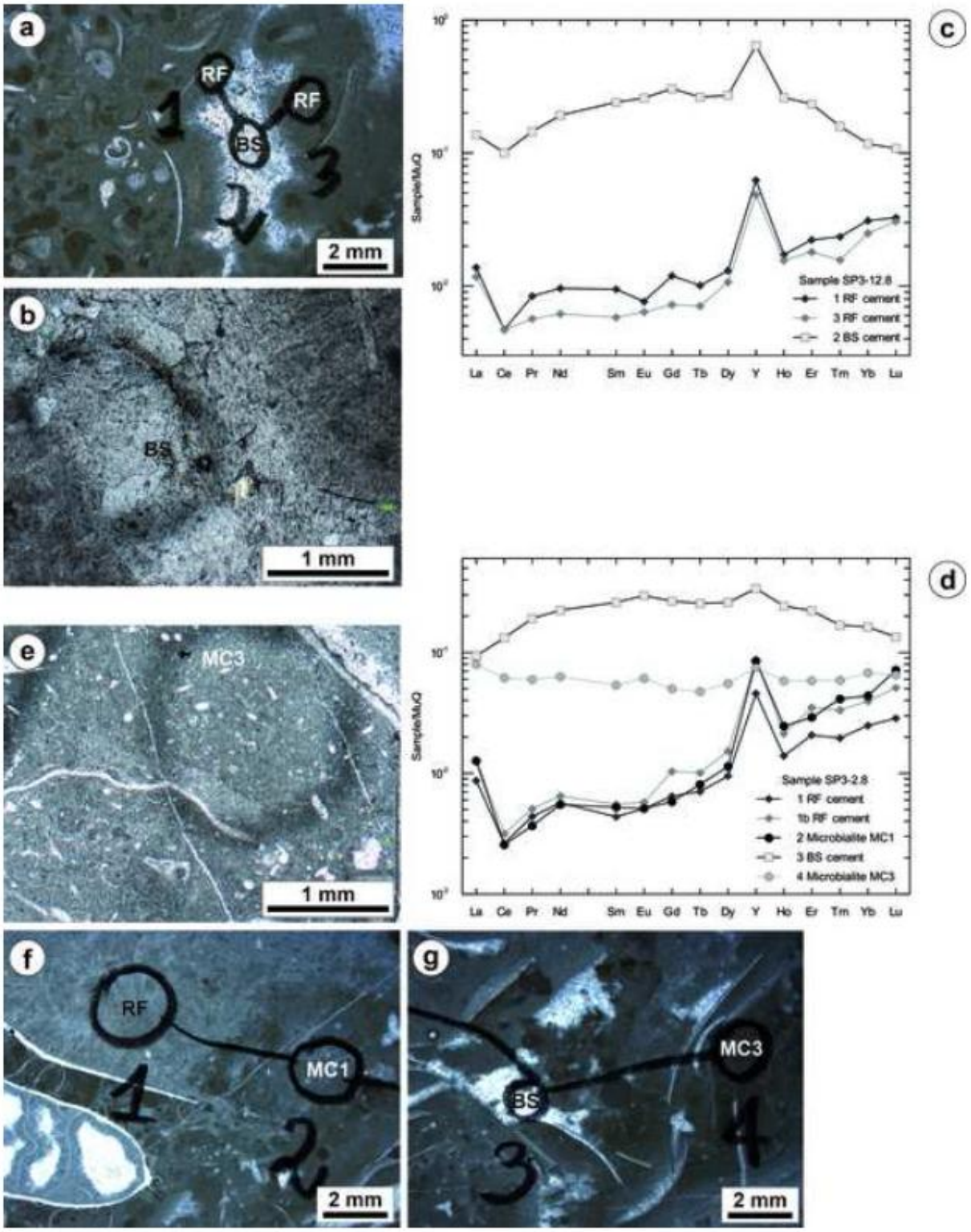
a
RF
RF
BS
1
2
3
2 mm
b
BS
1 mm
c
Sample/MuQ
Sample SP3-12.8
1 RF cement
3 RF cement
2 BS cement
La Ce Pr Nd Sm Eu Gd Tb Dy Y Ho Er Tm Yb Lu
d
Sample/MuQ
Sample SP3-2.8
1 RF cement
1b RF cement
2 Microbialite MC1
3 BS cement
4 Microbialite MC3
La Ce Pr Nd Sm Eu Gd Tb Dy Y Ho Er Tm Yb Lu
e
MC3
1 mm
f
RF
MC1
1
2
2 mm
g
MC3
BS
3
4
2 mm

Figure 4

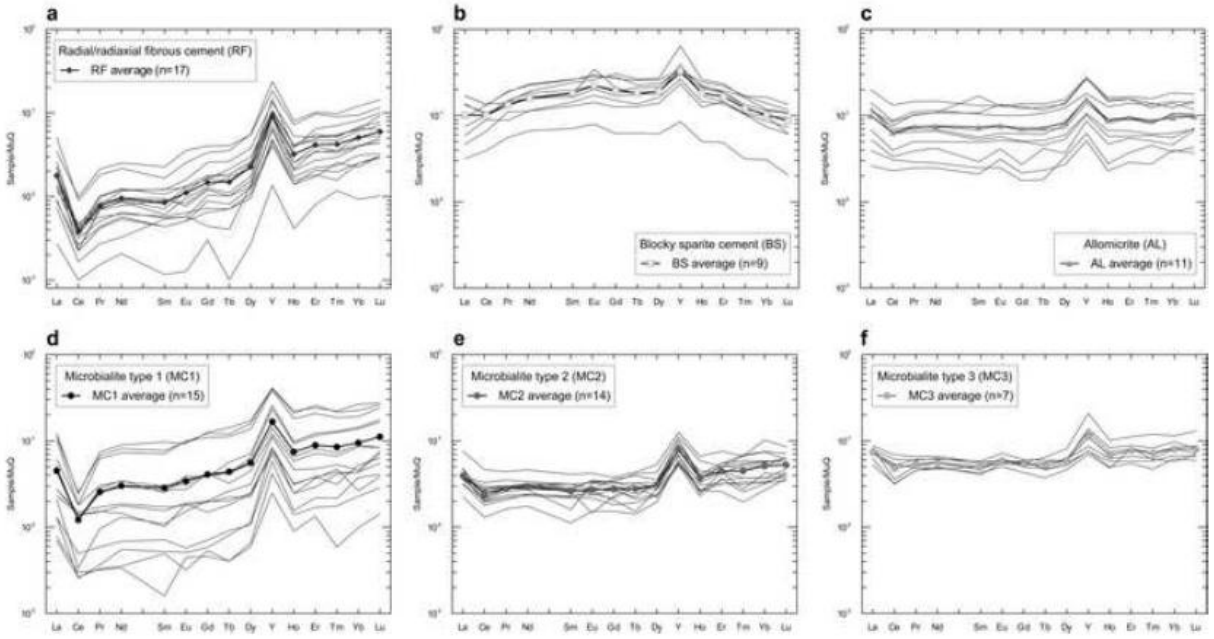

Figure 5

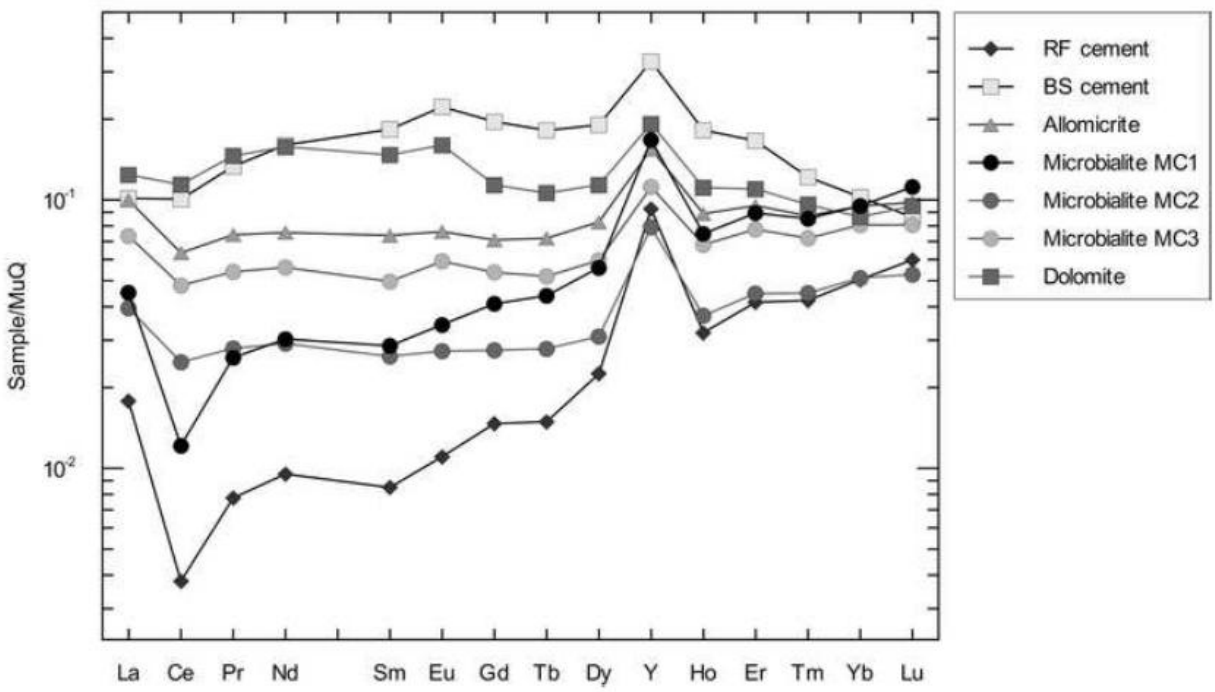

Figure 6

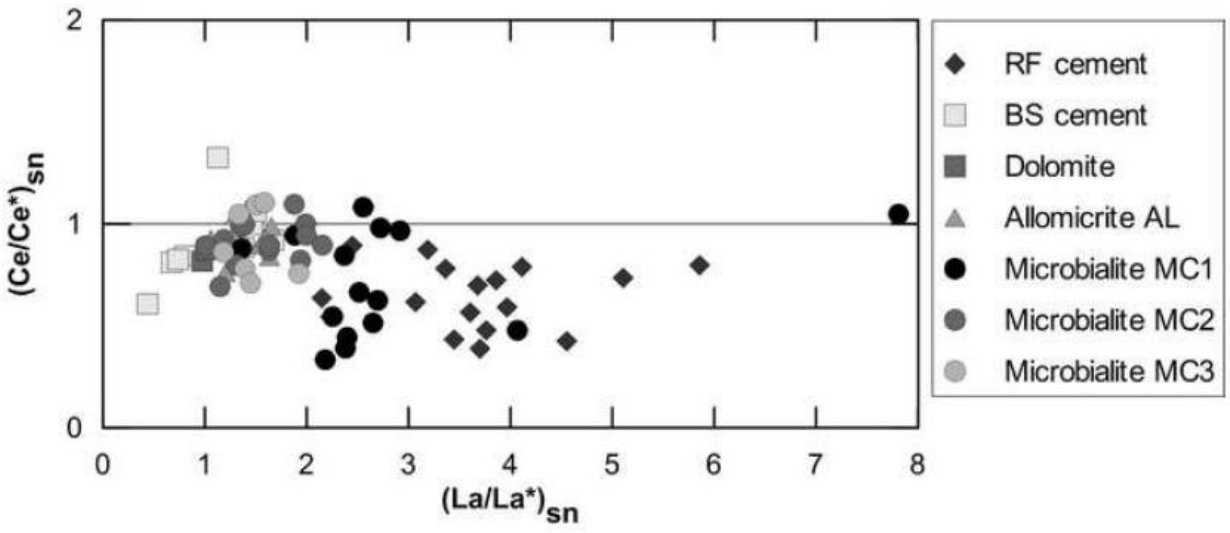

Figure 7

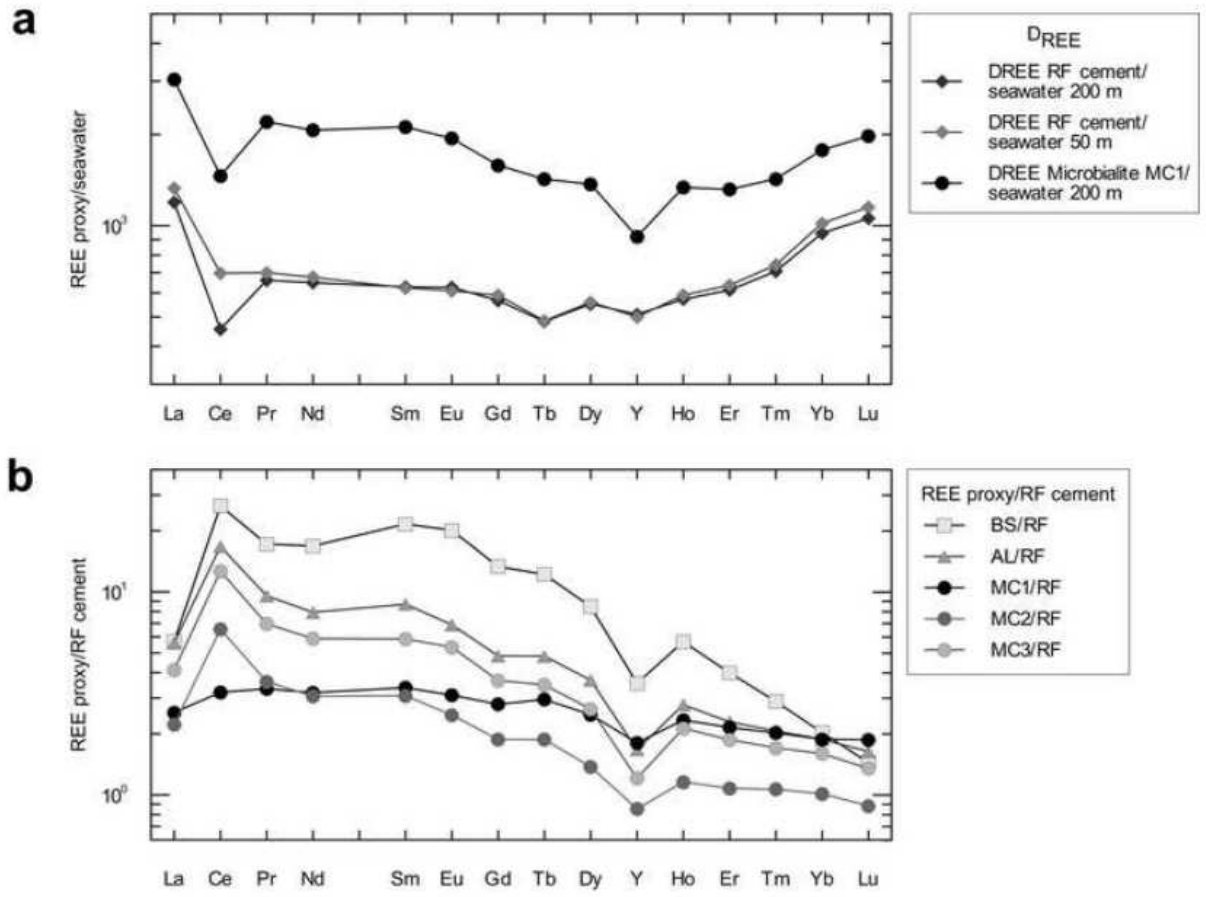

Figure 8

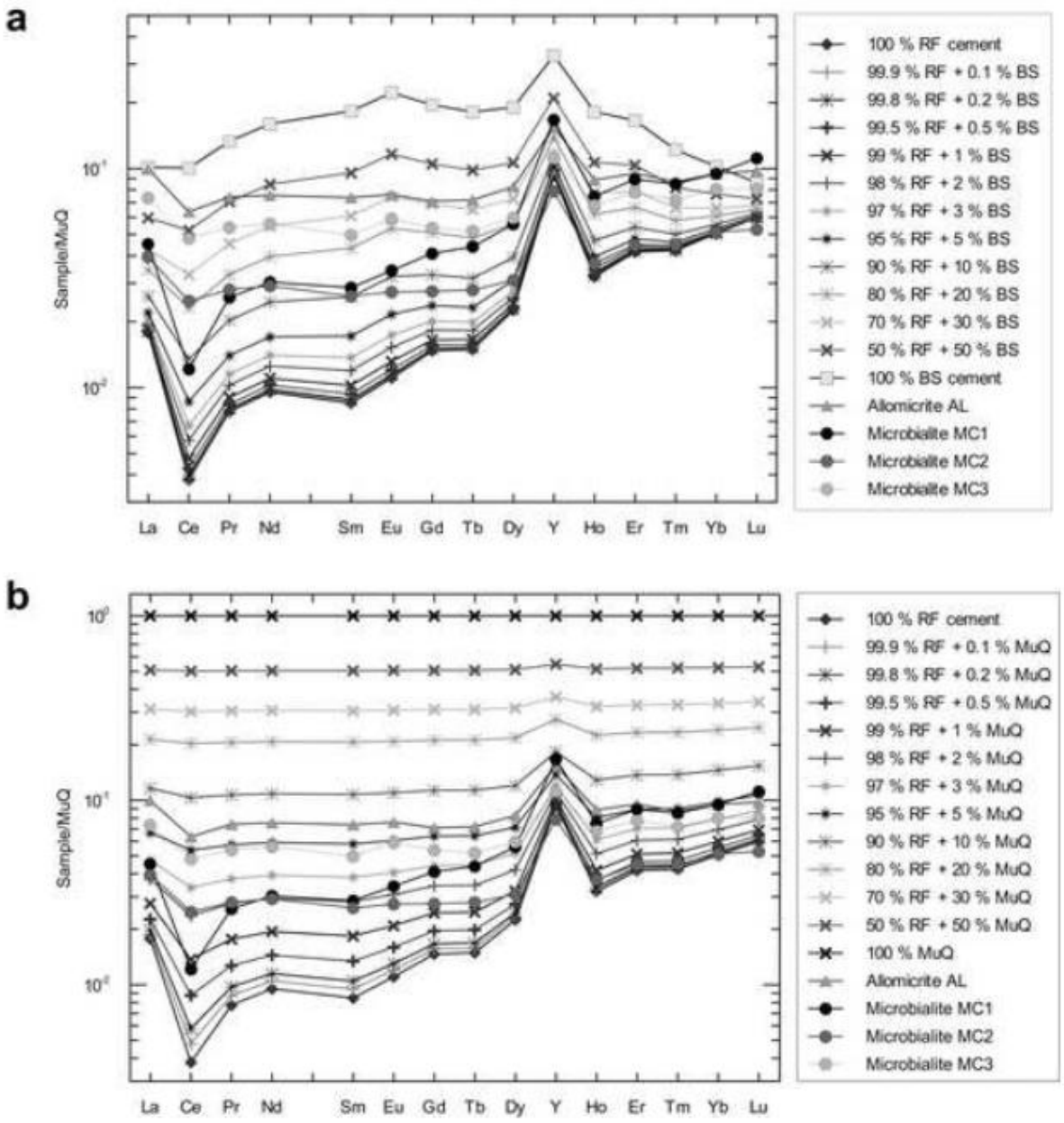

Figure 9

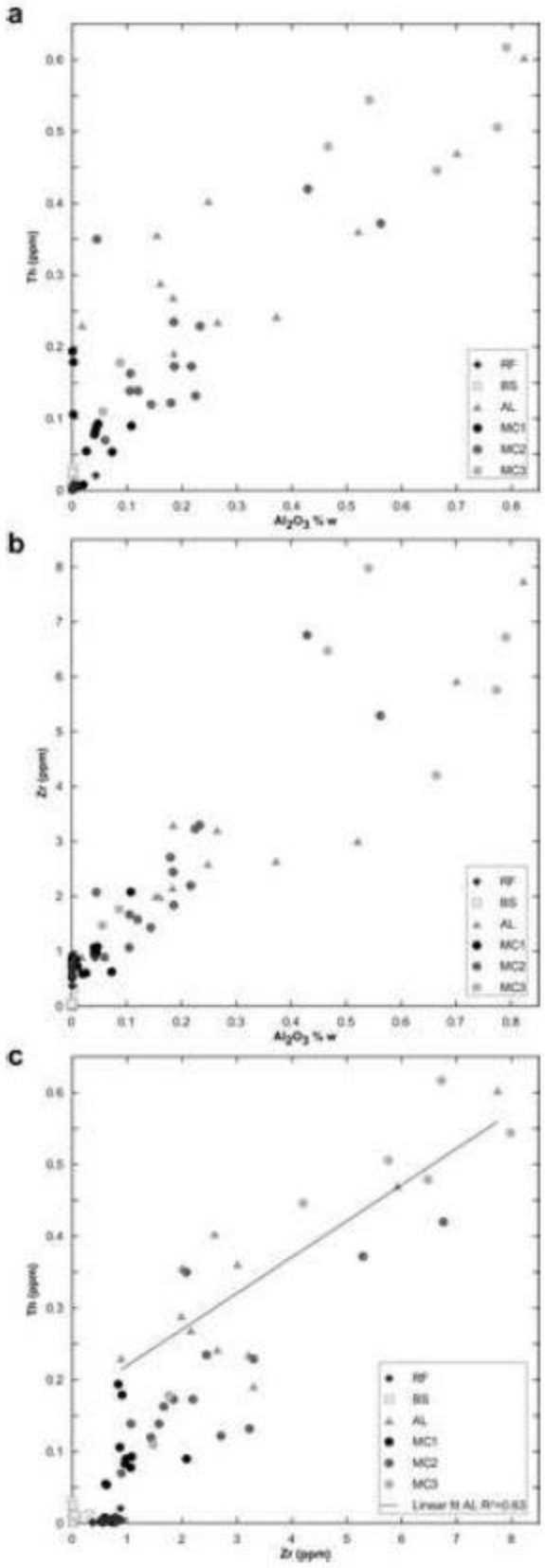

Figure 10

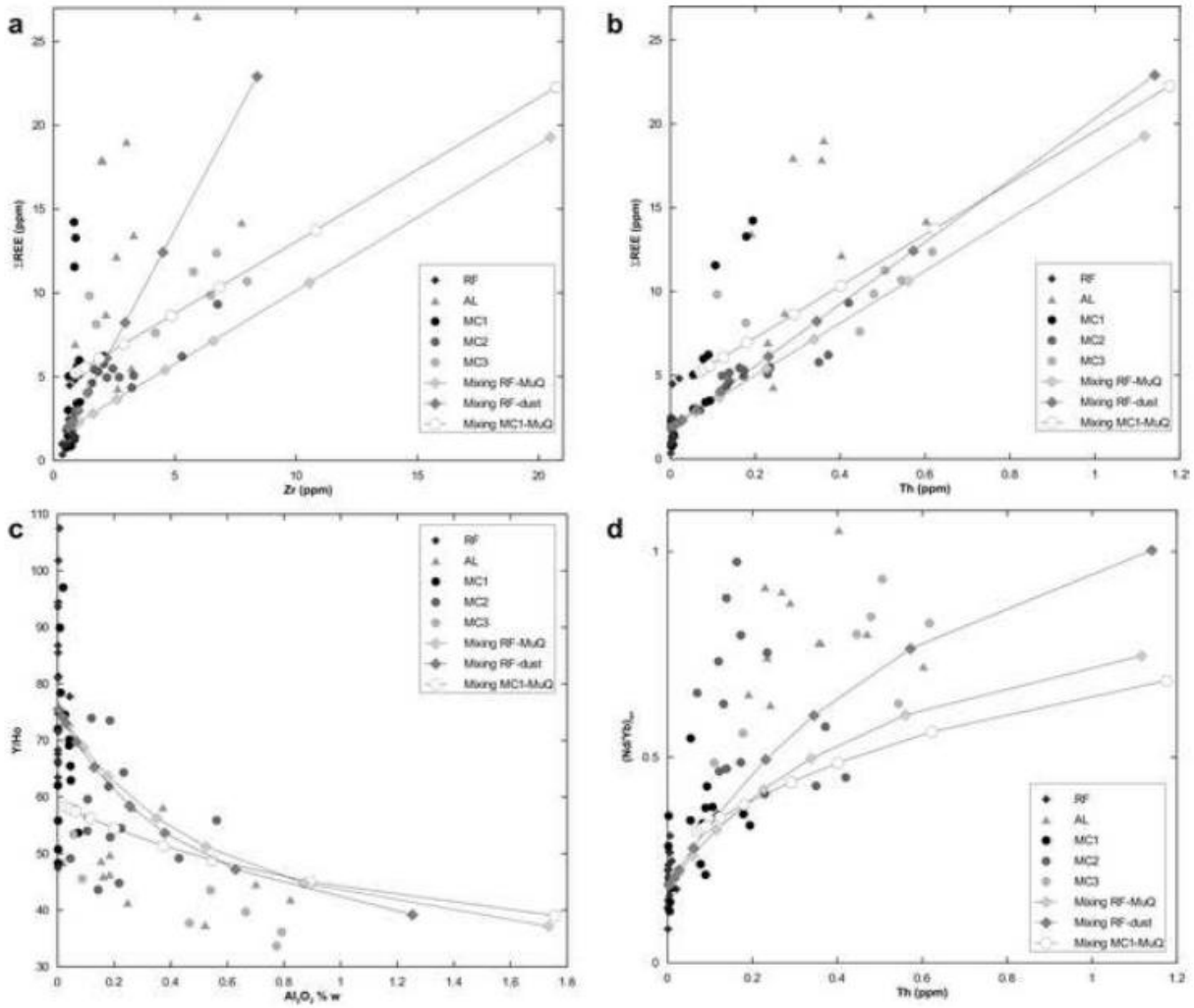

Figure 11

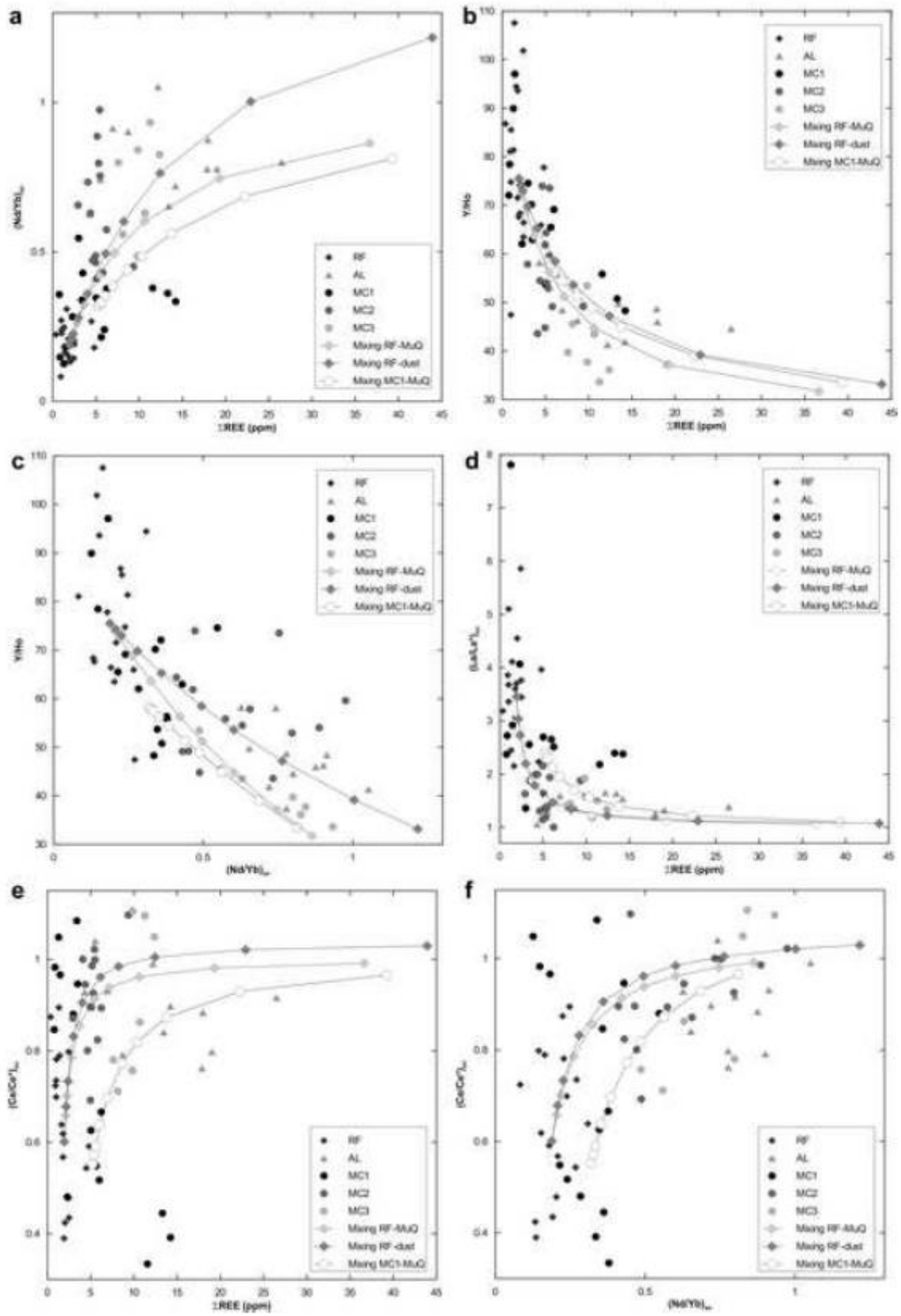
a
b
c
d
e
f
RF
AL
MC1
MC2
MC3
Mixing RF-MuQ
Mixing RF-dust
Mixing MC1-MuQ
ΣREE (ppm)
Y/Ho
(Nd/Yb)cn
(La/Lr)cn
(Ce/Ce*)cn

Figure 12

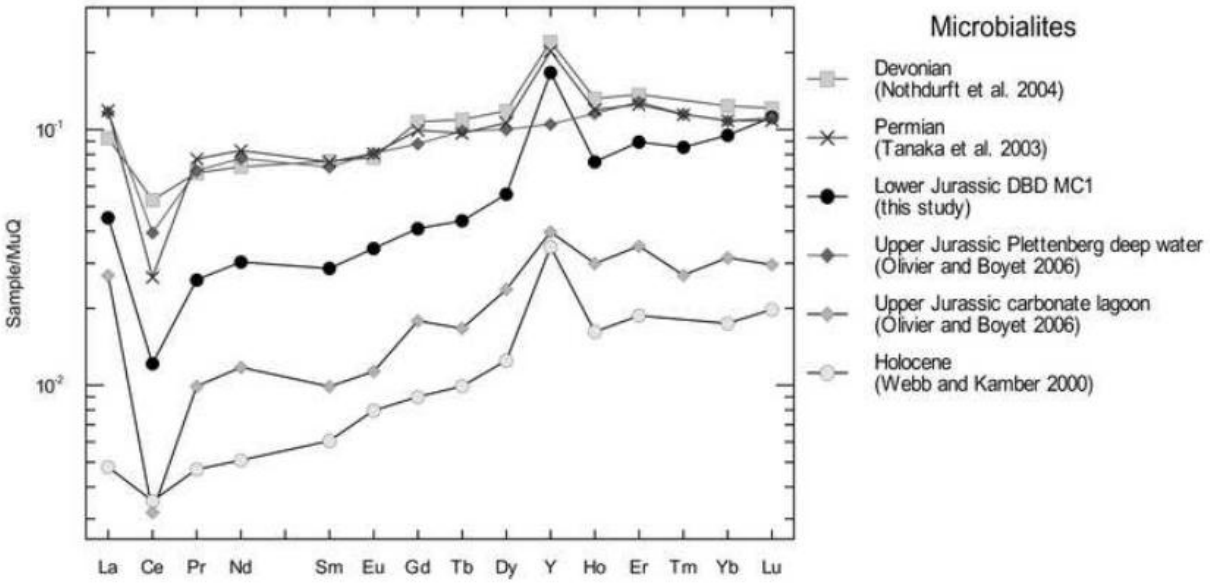

Figure 13

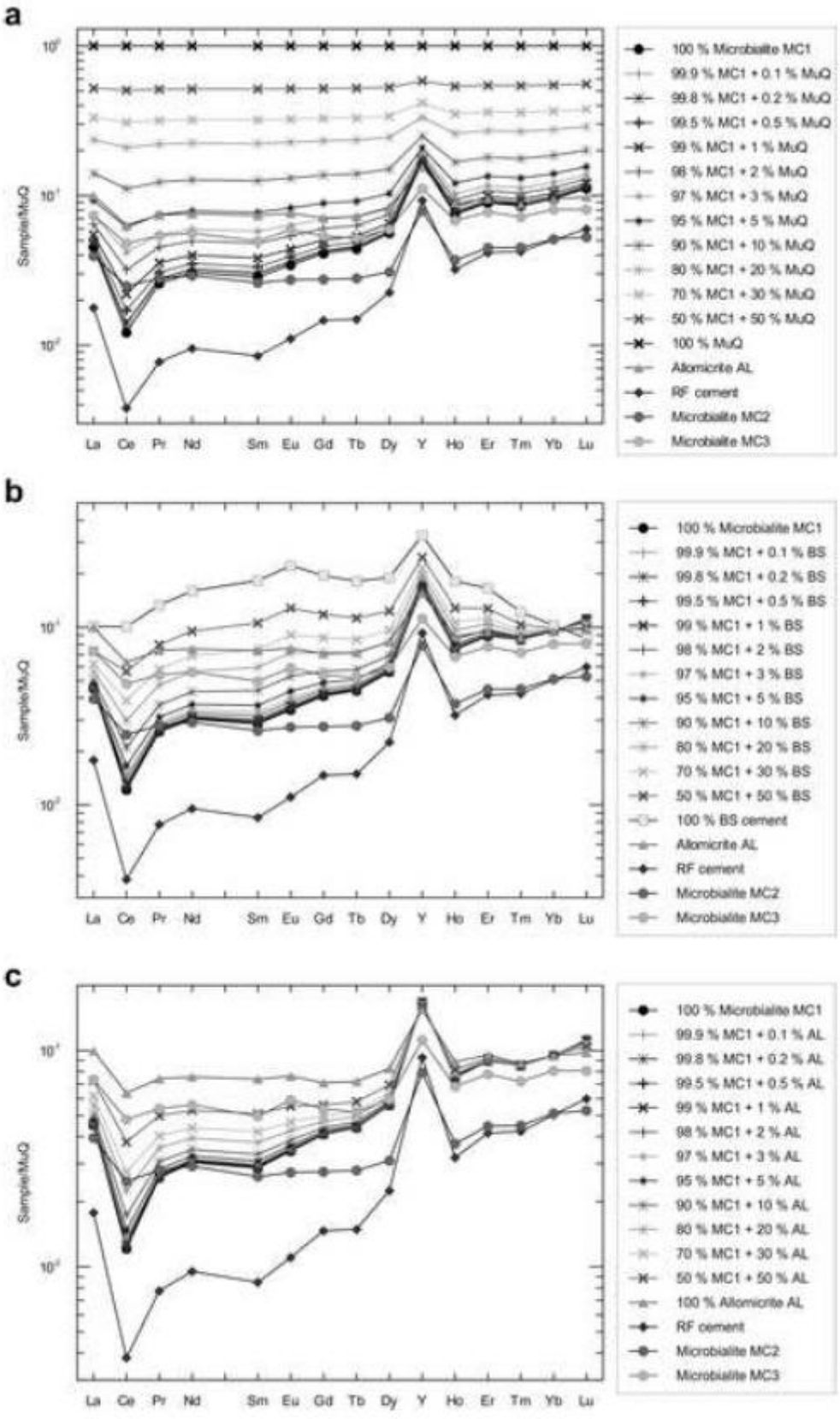
a
Sample/MuQ
La Ce Pr Nd Sm Eu Gd Tb Dy Y Ho Er Tm Yb Lu
100 % Microbialite MC1
99.9 % MC1 + 0.1 % MuQ
99.8 % MC1 + 0.2 % MuQ
99.5 % MC1 + 0.5 % MuQ
99 % MC1 + 1 % MuQ
98 % MC1 + 2 % MuQ
97 % MC1 + 3 % MuQ
95 % MC1 + 5 % MuQ
90 % MC1 + 10 % MuQ
80 % MC1 + 20 % MuQ
70 % MC1 + 30 % MuQ
50 % MC1 + 50 % MuQ
100 % MuQ
Allomicrite AL
RF cement
Microbialite MC2
Microbialite MC3
b
Sample/MuQ
La Ce Pr Nd Sm Eu Gd Tb Dy Y Ho Er Tm Yb Lu
100 % Microbialite MC1
99.9 % MC1 + 0.1 % BS
99.8 % MC1 + 0.2 % BS
99.5 % MC1 + 0.5 % BS
99 % MC1 + 1 % BS
98 % MC1 + 2 % BS
97 % MC1 + 3 % BS
95 % MC1 + 5 % BS
90 % MC1 + 10 % BS
80 % MC1 + 20 % BS
70 % MC1 + 30 % BS
50 % MC1 + 50 % BS
100 % BS cement
Allomicrite AL
RF cement
Microbialite MC2
Microbialite MC3
c
Sample/MuQ
La Ce Pr Nd Sm Eu Gd Tb Dy Y Ho Er Tm Yb Lu
100 % Microbialite MC1
99.9 % MC1 + 0.1 % AL
99.8 % MC1 + 0.2 % AL
99.5 % MC1 + 0.5 % AL
99 % MC1 + 1 % AL
98 % MC1 + 2 % AL
97 % MC1 + 3 % AL
95 % MC1 + 5 % AL
90 % MC1 + 10 % AL
80 % MC1 + 20 % AL
70 % MC1 + 30 % AL
50 % MC1 + 50 % AL
100 % Allomicrite AL
RF cement
Microbialite MC2
Microbialite MC3

Figure 14

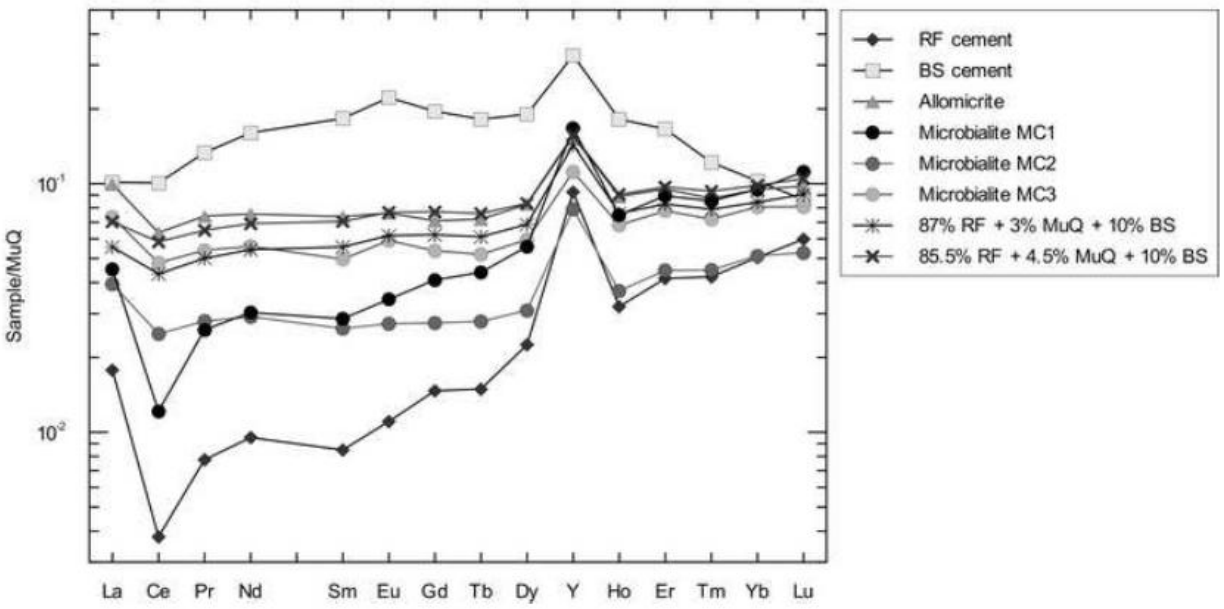

Figure 15

Table 1

	$\delta^{13}C$ ‰ V-PDB	$\delta^{18}O$ ‰ V-PDB
Radial/radiaxial fibrous cement (3 samples)		
Mean	2.3	-1.6
St Dev	0.1	0.3
max	2.4	-1.4
min	2.2	-1.9
Blocky sparite cement (4 samples)		
Mean	2.1	-5.5
St Dev	0.4	0.4
max	2.5	-5.1
min	1.5	-6.0
Allomicrite + grains (11 samples)		
Mean	1.9	-3.9
St dev	0.5	0.9
max	2.3	-2.2
min	0.6	-5.3
Microbial carbonate (12 samples)		
Mean	2.4	-2.7
St dev	0.3	0.3
max	2.6	-1.9
min	1.6	-3.0
Brachiopods (7 samples)		
Mean	2.2	-2.7
St dev	0.7	0.3
max	3.7	-2.4
min	1.5	-3.3
Dolomite in void (1 sample)	0.4	-5.5

Table 2

REE+Y (ppm)	Mean RF cement (n=17)	SD RF cement	Mean BS cement (n=9)	SD BS cement	Mean allomicrite AL (n=11)	SD AL	Mean microbial carbonate MC 1 (n=15)	SD MC 1	Mean microbial carbonate MC 2 (n=14)	SD MC 2	Mean microbial carbonate MC 3 (n=7)	SD MC 3	Mean raplacive dolomite DOL (n=2)	SD DOL
La	0.578	0.369	3.296	1.702	3.240	1.623	1.471	1.246	1.284	0.396	2.385	0.403	4.033	0.149
Ce	0.270	0.168	7.159	2.302	4.513	2.260	0.864	0.535	1.767	0.576	3.413	1.065	8.108	0.012
Pr	0.066	0.043	1.128	0.370	0.627	0.323	0.219	0.202	0.237	0.056	0.456	0.070	1.235	0.036
Nd	0.313	0.197	5.271	1.801	2.485	1.292	0.998	0.940	0.959	0.216	1.845	0.255	5.195	0.049
Sm	0.058	0.036	1.259	0.444	0.507	0.329	0.197	0.203	0.180	0.050	0.342	0.047	1.012	0.016
Eu	0.017	0.013	0.349	0.130	0.120	0.064	0.054	0.054	0.043	0.012	0.093	0.011	0.252	0.012
Gd	0.093	0.065	1.244	0.506	0.451	0.278	0.261	0.272	0.175	0.044	0.342	0.038	0.723	0.037
Tb	0.015	0.011	0.180	0.065	0.071	0.041	0.044	0.044	0.028	0.009	0.051	0.009	0.105	0.001
Dy	0.133	0.089	1.121	0.385	0.487	0.276	0.329	0.329	0.182	0.052	0.351	0.064	0.671	0.052
Y	2.950	1.815	10.459	4.732	4.925	2.690	5.324	4.363	2.518	0.769	3.559	1.608	6.120	0.352
Ho	0.039	0.025	0.222	0.081	0.108	0.061	0.091	0.088	0.045	0.016	0.083	0.023	0.136	0.009
Er	0.140	0.091	0.560	0.188	0.321	0.172	0.301	0.280	0.151	0.043	0.262	0.067	0.370	0.079
Tm	0.022	0.013	0.062	0.022	0.044	0.022	0.043	0.037	0.023	0.009	0.037	0.012	0.049	0.001
Yb	0.164	0.095	0.333	0.124	0.308	0.162	0.309	0.261	0.166	0.069	0.262	0.066	0.281	0.013
Lu	0.029	0.018	0.042	0.017	0.048	0.022	0.055	0.043	0.026	0.007	0.040	0.012	0.047	0.006
ΣREE (ppm)	1.938	1.184	22.226	7.456	13.330	6.742	5.234	4.444	5.266	1.418	9.961	1.681	22.213	0.388
Y/Ho	78.565	15.370	47.076	9.748	47.338	6.462	67.131	13.961	56.817	9.323	41.404	6.724	45.182	0.466
Al_2O_3 % weight	0.004	0.010	0.001	0.001	0.330	0.251	0.029	0.031	0.200	0.141	0.483	0.304	0.027	0.011
Zr (ppm)	0.632	0.170	0.060	0.103	3.225	1.952	0.897	0.372	2.608	1.641	4.912	2.520	4.156	2.042
Th (ppm)	0.004	0.005	0.012	0.010	0.332	0.124	0.070	0.061	0.203	0.106	0.411	0.191	0.014	0.002
Mn (ppm)	106.577	64.020	538.267	420.708	241.173	73.585	145.031	77.146	224.686	69.261	179.540	66.768	125.150	9.546
U (ppm)	0.060	0.012	0.004	0.003	0.521	0.553	0.066	0.016	0.109	0.074	0.328	0.277	0.591	0.246

(REE+Y)sn MUQ normalized	Mean RF cement	SD RF cement	Mean BS cement	SD BS cement	Mean allomicrite AL	SD AL	Mean microbial carbonate MC 1	SD MC 1	Mean microbial carbonate MC 2	SD MC2	Mean microbial carbonate MC 3	SD MC 3	Mean dolomite (DOL)	SD DOL
La	0.018	0.011	0.101	0.052	0.100	0.050	0.045	0.038	0.040	0.012	0.073	0.012	0.124	0.005
Ce	0.004	0.002	0.101	0.032	0.063	0.032	0.012	0.008	0.025	0.008	0.048	0.015	0.114	0.000
Pr	0.008	0.005	0.133	0.044	0.074	0.038	0.026	0.024	0.028	0.007	0.054	0.008	0.146	0.004
Nd	0.010	0.006	0.160	0.055	0.076	0.039	0.030	0.029	0.029	0.007	0.056	0.008	0.158	0.001
Sm	0.008	0.005	0.183	0.065	0.074	0.048	0.029	0.029	0.026	0.007	0.050	0.007	0.147	0.002
Eu	0.011	0.008	0.222	0.083	0.076	0.041	0.034	0.034	0.027	0.008	0.059	0.007	0.160	0.008
Gd	0.015	0.010	0.196	0.080	0.071	0.044	0.041	0.043	0.028	0.007	0.054	0.006	0.114	0.006
Tb	0.015	0.011	0.182	0.066	0.072	0.042	0.044	0.045	0.028	0.009	0.052	0.009	0.106	0.001
Dy	0.023	0.015	0.190	0.065	0.083	0.047	0.056	0.056	0.031	0.009	0.060	0.011	0.114	0.009
Y	0.093	0.057	0.328	0.149	0.155	0.084	0.167	0.137	0.079	0.024	0.112	0.050	0.192	0.011

Ho	0.032	0.021	0.182	0.067	0.089	0.050	0.075	0.072	0.037	0.013	0.068	0.019	0.111	0.008
Er	0.042	0.027	0.166	0.056	0.095	0.051	0.089	0.083	0.045	0.013	0.078	0.020	0.110	0.024
Tm	0.042	0.025	0.122	0.043	0.087	0.044	0.085	0.073	0.045	0.017	0.072	0.024	0.096	0.003
Yb	0.051	0.029	0.102	0.038	0.095	0.050	0.095	0.080	0.051	0.021	0.081	0.020	0.086	0.004
Lu	0.060	0.036	0.086	0.035	0.098	0.045	0.112	0.089	0.053	0.015	0.081	0.024	0.095	0.013
(Nd/Yb)sn	0.199	0.059	1.637	0.387	0.804	0.124	0.311	0.113	0.623	0.183	0.725	0.219	1.828	0.100
(Dy/Yb)sn	0.435	0.093	1.904	0.340	0.860	0.131	0.544	0.180	0.640	0.125	0.751	0.079	1.320	0.161
(Pr/Yb)sn	0.160	0.051	1.365	0.311	0.790	0.110	0.273	0.120	0.597	0.178	0.698	0.164	1.691	0.126
(Pr/Tb)sn	0.653	0.328	0.754	0.111	1.094	0.207	0.646	0.146	1.063	0.304	1.063	0.219	1.376	0.022
Ce anomaly	0.646	0.158	0.920	0.199	0.889	0.086	0.718	0.258	0.918	0.103	0.909	0.170	0.846	0.040
La anomaly	3.652	0.954	1.089	0.438	1.391	0.193	2.851	1.488	1.570	0.369	1.482	0.233	0.995	0.032
Eu anomaly	1.084	0.205	1.229	0.270	1.106	0.154	1.085	0.335	1.065	0.276	1.179	0.091	1.215	0.961
Gd anomaly	1.293	0.416	1.057	0.111	0.963	0.091	1.082	0.194	1.042	0.188	1.062	0.125	0.051	0.045

Highlights manuscript

REE patterns of microbial carbonate and cements from Sinemurian (Lower Jurassic) siliceous sponge mounds (Djebel Bou Dahar, High Atlas, Morocco)

Giovanna Della Porta, Gregory E. Webb & Iain McDonald

1. Importance of analysing specific carbonate components for REE+Y patterns
2. Oxygenated seawater patterns are preserved in marine cement and some microbialites
3. Deviations from marine REE+Y due to sedimentary sources and diagenetic processes
4. REEs affected by incorporation of marine particulate matter scavenging LREEs
5. Microbial mounds accumulated in well-oxygenated water not at Oxygen Minimum Zone